



Cyclic Axial Compression Behavior of FRP-Confined Seawater Sea-Sand Concrete-Filled Stainless Steel Tube Stub Columns

Jun-Jie Zeng^{1,2*}, JinJing Liao¹, Wen-Feng Liang¹, Yong-Chang Guo^{1*}, Jie-Kai Zhou¹, Jia-Xiang Lin¹ and Kang Yan¹

¹School of Civil and Transportation Engineering, Guangdong University of Technology, Guangzhou, China, ²Department of Civil and Environmental Engineering, University of Macau, Macau, Macau SAR, China

OPEN ACCESS

Edited by:

Xiaoshan Lin,
RMIT University, Australia

Reviewed by:

Yang Wei,
Nanjing Forestry University, China
Yulei Bai,
Beijing University of Technology,
China

*Correspondence:

Jun-Jie Zeng
jjzeng@gdut.edu.cn
Yong-Chang Guo
guoyc@gdut.edu.cn

Specialty section:

This article was submitted to
Structural Materials,
a section of the journal
Frontiers in Materials

Received: 09 February 2022

Accepted: 23 February 2022

Published: 23 March 2022

Citation:

Zeng J-J, Liao J, Liang W-F, Guo Y-C,
Zhou J-K, Lin J-X and Yan K (2022)
Cyclic Axial Compression Behavior of
FRP-Confined Seawater Sea-Sand
Concrete-Filled Stainless Steel Tube
Stub Columns.
Front. Mater. 9:872055.
doi: 10.3389/fmats.2022.872055

Concrete-filled steel tube (CFST) columns have been widely used in onshore constructions. To extend its applications to coastal/offshore structures and meanwhile relieve the overexploitation on freshwater and river sand, an FRP-confined seawater sea-sand concrete-filled stainless steel tube (F-SSCFSSST) column is proposed. The cyclic axial compressive behavior of this newly proposed column was investigated in this study. A total of 22 specimens (including nine pairs of specimens for cyclic compression and four individual specimens for monotonic compression) were tested. Most importantly, the influences of three loading patterns (i.e., single full unloading/reloading, repeated full unloading/reloading, and mixed of repeated full and partial unloading/reloading) were studied. The results showed that although all F-SSCFSSST specimens failed from FRP rupture in the mid-height area, the FRP rupture was less fierce for specimens with repeated internal unloading/reloading cycles. Similar to the FRP-confined concrete, the envelope curve of cyclic axial load-strain response matched closely with the monotonic compression curve for a particular specimen. However, the unloading curve was less curly compared with that of a typical FRP-confined concrete. The confinement effect provided by the FRP jacket was much stronger than that by the stainless steel tube. Although Lam and Teng's model, which is proposed for the FRP-confined concrete, could provide satisfactory estimations for strain recovery ratios and stress deterioration ratios, it underestimated the envelope plastic strains by 20%.

Keywords: fiber-reinforced polymer (FRP), seawater sea-sand concrete (SSC), stainless steel tube (SST), axial cyclic compression, plastic strain

HIGHLIGHT

- Confinement by the FRP jacket is much stronger than that of the stainless steel tube.
- Different cyclic loading protocols have little effect in ultimate load carrying capacity.
- The unloading curve is less curly compared with that of the FRP-confined concrete, and thus Lam and Teng's model underestimates the envelope plastic strain by 20%.

- Lam and Teng's model can still yield satisfactory strain recovery ratio and stress deterioration ratio.

INTRODUCTION

Concrete-filled steel tube (CFST) columns have been increasingly used in onshore structures. The confinement provided by the outer steel tube can restrain the dilation of the concrete core, and thus enhance the axial load carrying capacity and ductility of the column (Ellobody et al., 2006; Wang et al., 2013; Hou et al., 2014; Wang et al., 2017; Geng et al., 2020). A number of studies have delved into the compressive behavior of CFST columns with different in-filled concrete strength, steel tube strength, and steel tube shapes (Xiao et al., 2005; Xiong et al., 2017; Wang et al., 2018; Wei et al., 2019; Ouyang et al., 2020; Liao et al., 2021a). It is generally concluded that the specimens exhibit a load plateau after steel tube yielding (Xiao et al., 2005; Xiong et al., 2017; Wang et al., 2018; Wei et al., 2019; Ouyang et al., 2020; Liao et al., 2021a). However, when utilized in coastal/offshore constructions (e.g., cross-sea bridges), the traditional CFST columns have two major drawbacks. First, corrosion issues may not only emanate from the outer surface of the steel tube which contacts seawater directly but also arise from the inner surface. To date, seawater sea-sand concrete (SSC) has been widely used in maritime constructions as a substitution for conventional concrete due to two advantages: 1) relief of over-exploitation on freshwater and river-sand; and 2) significant cutdown on raw material transportation costs (Zeng et al., 2020a; Zeng et al., 2020b; Ye et al., 2021). As a result, chloride ions in SSC will also pose corrosion threats to the inner surface of steel tubes. Second, the composite action between the steel tube and concrete core is weak because they have different Poisson's ratio values (typically 0.3 for the steel tube and 0.2 for the concrete) (Zeng et al., 2020c; Zeng et al., 2021a). This suggests that during compression, delamination failure and the following steel tube local buckling would impair the strength and ductility of CFST columns (Zeng et al., 2020c; Zeng et al., 2021a).

To resolve the corrosion drawback, the stainless steel tube (SST) has been proposed to replace the carbon steel tube in CFST columns (Guo et al., 2019; Tan et al., 2020; Qiao et al., 2021). Stainless steel not just has better corrosion resistance than carbon steel but also has improved fire and fatigue performance (Qiao et al., 2021). In terms of mechanical properties, stainless steel usually exhibits significant strain hardening characteristics and does not show a yield plateau as carbon steel (Qiao et al., 2021). However, due to the less carbon content, stainless steel is softer in strength than carbon steel (Han et al., 2019). Investigations on confinement performance of the SST are also abundant (Guo et al., 2019; Han et al., 2019; Dai et al., 2020; Tan et al., 2020; Qiao et al., 2021). These investigations can be divided into two groups, one is for concrete-filled stainless steel tube (CFSST) columns in which an SST not only provides confinement but also resists the axial load; the other one is called stainless steel tube confined concrete (SSTCC) in which an SST does not participate in carrying axial load (Tan et al., 2020). It is interesting to find that the load-carrying capacity of an SSTCC column is greater than that of a CFSST column (Tan et al., 2020), and the ductility of an SSTCC column can also be improved as the local buckling of the SST is delayed (Qiao et al., 2021). The second major drawback (i.e., weak composite action) mentioned above can be remedied by applying an external fiber-reinforced polymer (FRP) jacket over CFST columns. The FRP material has a very high strength-to-weight ratio and has been extensively used in civil engineering (Wu and Jiang, 2013; Liao et al., 2021b; Wei et al., 2021; Zhou et al., 2021; Liao et al., 2022a; Zeng et al., 2022a; Liao et al., 2022b; Zeng et al., 2022b; Mo et al., 2022; Pan et al., 2022). During axial compression, FRP confinement not only improves the composite action between the steel tube and concrete core but also delays (or to some extent prevent) the outward bulging of the steel tube. As a result, both strength and ductility of the specimen can be enhanced. The typical axial compressive response of an FRP-confined CFST column consists of a load hardening branch after the FRP jacket is fully activated (Tao et al., 2007; Gholampour and Ozbakkaloglu, 2018; Zhang et al., 2019; Zhang et al., 2020a; Wei et al., 2020), which is different from the response of a CFST column. A

TABLE 1 | Specimen details.

Specimen	CFRP jacket		Stainless steel tube		Loading scheme
	Layer	t_f (mm)	D (mm)	t_s (mm)	
C-SST2-F2-L1-a,b	2	0.334	219	2	Cyclic L1
C-SST2-F2-L2-a,b	2	0.334	219	2	Cyclic L2
C-SST4-F0-L1-a,b	0	0	219	4	Cyclic L1
C-SST4-F0-L2-a,b	0	0	219	4	Cyclic L2
C-SST4-F2-L1-a,b	2	0.334	219	4	Cyclic L1
C-SST4-F2-L2-a,b	2	0.334	219	4	Cyclic L2
C-SST4-F2-L3-a,b	2	0.334	219	4	Cyclic L3
C-SST4-F4-L1-a,b	4	0.668	219	4	Cyclic L1
C-SST4-F4-L2-a,b	4	0.668	219	4	Cyclic L2
M-SST2-F2	2	0.334	219	2	Monotonic
M-SST4-F0	0	0	219	4	Monotonic
M-SST4-F2	2	0.334	219	4	Monotonic
M-SST4-F4	4	0.668	219	4	Monotonic

Note: D and t_s —outer diameter and wall thickness of the SST, respectively; t_f —thickness of the CFRP jacket.

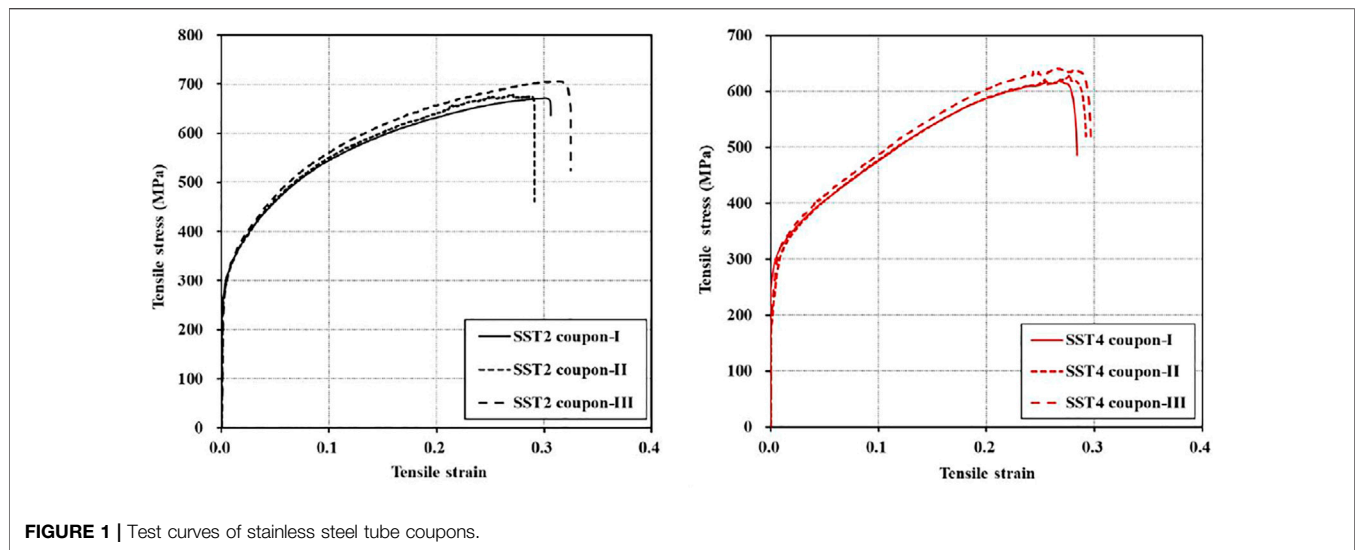


FIGURE 1 | Test curves of stainless steel tube coupons.

TABLE 2 | Material properties of stainless steel tubes.

Tube specification	Thickness (mm)	0.2% proof stress, $f_{0.2}$ (MPa)	Ultimate tensile stress, $f_{s,u}$ (MPa)	Elastic modulus, E_s (GPa)	Poisson's ratio, μ_s
SST2	2	304.9	679.6	188.4	0.29
SST4	4	294.9	626.3	182.7	0.30

TABLE 3 | Mix proportions of seawater sea-sand concrete.

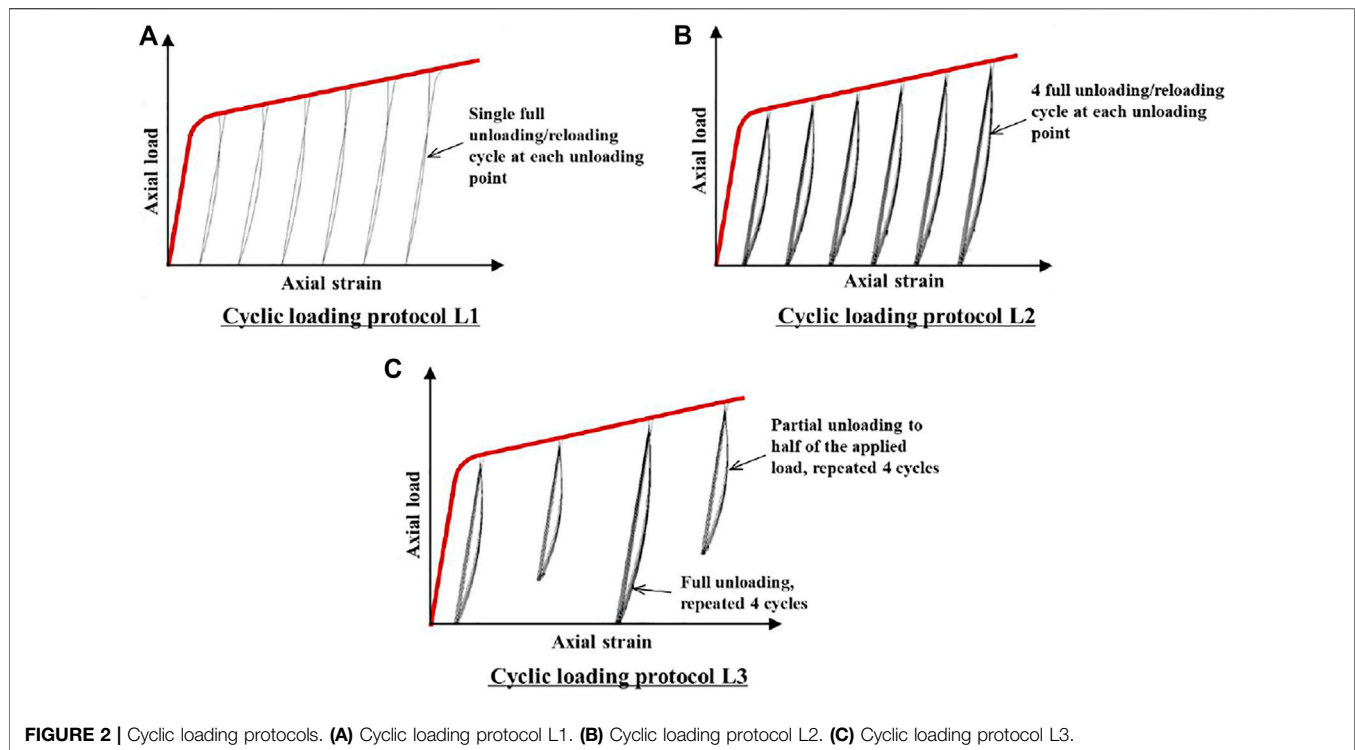
Mix material	Ordinary Portland cement (P.O.42.5R)	Sea-sand	Coarse aggregates (granites; maximum particle size 20 mm)	Simulated seawater
Proportion by weight	1	1.76	3.13	0.54

theoretical model has been proposed by Teng et al. (Teng et al., 2013) to predict the stress-strain behavior of the confined concrete in FRP-confined CFST columns. Apparently, the application of both the SST and FRP jacket can resolve the two major drawbacks at the same time. Currently, only Tang et al. (Tang et al., 2020) has conducted experimental research on FRP-confined concrete-filled SST columns. However, Tang et al.'s study (Tang et al., 2020) only focused on the monotonic compressive behavior.

To date, the majority of investigations on the cyclic compressive behavior of confined concrete are still concentrated on FRP-confined concrete (Lam and Teng, 2009; Ozbakkaloglu and Akin, 2011; Li and Wu, 2015). For example, Lam and Teng (Lam and Teng, 2009) have developed a stress-strain model for FRP-confined concrete under cyclic compression, including the predictions of a single unloading/reloading cycle at each prescribed unloading occasion, and multiple repeated internal unloading/reloading cycles at each prescribed unloading occasion. Li and Wu (Li and Wu, 2015) proposed another stress-strain model with simplified

mathematical forms. Ozbakkaloglu and Akin (Ozbakkaloglu and Akin, 2011) accounted for the impacts of concrete type on the model. To our best knowledge, only Yu et al. (Yu et al., 2014) and Zhang et al. (Zhang et al., 2020b) have studied the cyclic compressive stress-strain behavior of the FRP-confined CFST. Yu et al.'s model (Yu et al., 2014) is further developed on the basis of Lam and Teng's model (Lam and Teng, 2009), although the predictions of Yu et al.'s model (Yu et al., 2014) had high level of accuracy, the method was too complicated that it may be more suitable for computer programs. By contrast, Zhang et al.'s model (Zhang et al., 2020b) is a design-oriented model that has much simpler mathematical forms. It is of particular importance to gain in-depth understanding on the cyclic compressive behavior of the FRP-confined SSC-filled SST (F-SSCFSSST), which is fundamental for the reliable seismic design for the hybrid column form. Nevertheless, the cyclic axial compressive behavior of the F-SSCFSSST columns has not been explored yet.

In this light, axial cyclic compression tests were performed for F-SSCFSSST specimens in this study. The effects of SST thickness,



FRP thickness, and cyclic loading protocols were under investigation. In addition, the applicability and accuracy of Lam and Teng's model (Lam and Teng, 2009) were evaluated and discussed by analyzing three key parameters (plastic strain, strain recovery ratio, and stress deterioration ratio).

TEST PROGRAM

Specimen Details

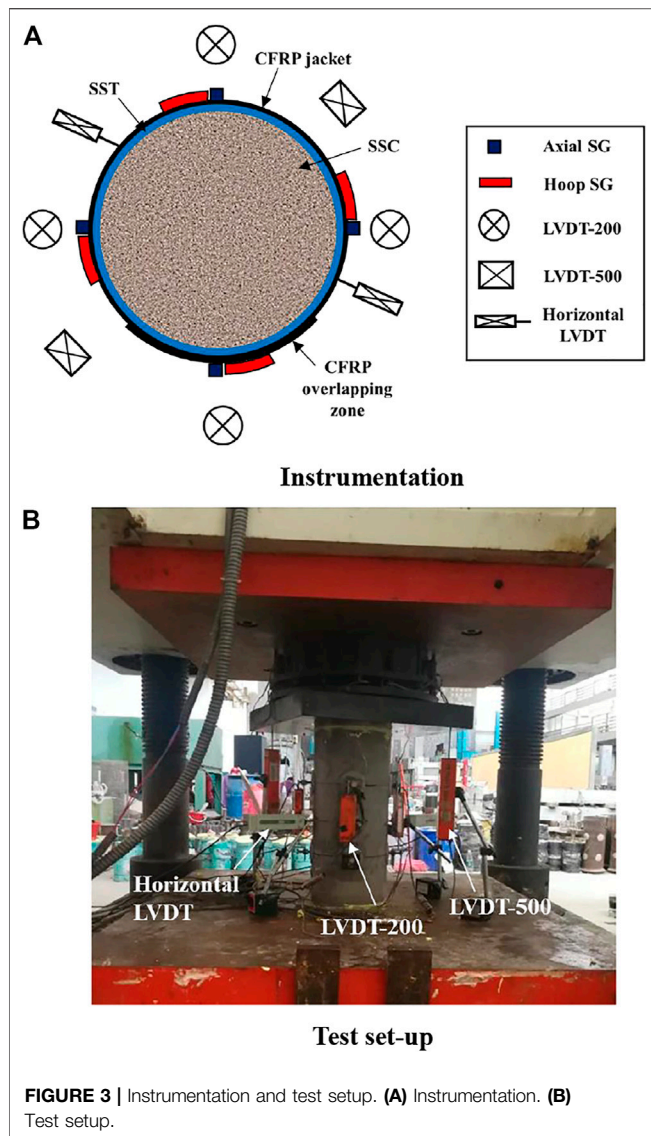
In total, 22 specimens, including nine pairs for cyclic axial compression (two duplicated specimens in a pair) and four individual specimens for monotonic axial compression, were fabricated and tested. All specimens had the same size (219 mm in outer diameter \times 500 mm in height) and were filled with the same batch of concrete (normal strength SSC). The nine pairs of specimens under cyclic compression can be divided into two groups as per the SST thickness (2 and 4 mm, denoted by "SST2" and "SST4", respectively). The majority of the cyclic compression specimens were in the SST4 group, in which three external FRP jacketing configurations were prepared: 1) no FRP confinement (denoted by "F0"); 2) confined with 2-ply CFRP jackets (denoted by "F2"); 3) confined with 4-ply CFRP jackets (denoted by "F4"). For comparison, only 2-ply CFRP external wrapping was applied to the specimens in group SST2. Therefore, there were four primary F-SSCFSSST specimen configurations (the SSCFSST specimen with no FRP confinement can be seen as a special case of the F-SSCFSSST specimen). For each primary specimen configuration, two loading protocols were applied:

they are single full unloading/reloading cycle at each prescribed unloading point (denoted by "L1") and four repeated full unloading/reloading cycles at each prescribed unloading point (denoted by "L2"). In addition, an additional loading protocol (i.e., combination of repeated full and partial unloading/reloading cycles at each prescribed unloading point, denoted by "L3") was considered for the F-SSCFSSST specimen with a 4-mm-thick SST and 2-ply CFRP jacket. The three types of loading protocols are elaborated in *Loading Protocol* Section. Correspondingly, the four primary F-SSCFSSST specimen configurations were also tested under monotonic axial compression, serving as the references for their counterparts under cyclic compression. The specimen details are given in **Table 1**.

The specimens were named in the following convention: "loading type (i.e., "M" for monotonic compression, "C" for cyclic compression)"—"SST tube specification (i.e., SST2 and SST4)"—"CFRP confinement configuration (i.e., F0, F2, and F4)"—"loading protocol for cyclic compression (i.e., L1, L2, and L3)"—"identifications for the two duplicates (i.e., letters "a" and b)". For example, C-SST4-F2-S4-L2-b signifies that the specimen is the second duplicate in the pair of the F-SSCFSSST specimens with the 4-mm-thick SST and 2-ply CFRP jacket, which is subjected to cyclic axial compression of loading protocol L2.

Material Properties

The specimens were made of three materials: CFRP sheets, SSTs, and SSC. The CFRP sheets were purchased from Toray Industries, Inc., which were manufactured with a nominal thickness of 0.167 mm per layer. Standard coupons tests as per



ASTM D3039/D3039M-17 (ASTM D3039/D3039M-17, 2014) were performed for five CFRP samples. The tensile strength (f_f), tensile rupture strain (ϵ_f), and elastic modulus (E_f) of the CFRP sheet were taken as the mean values of the five samples to be 4,324.2 MPa, 0.0185, and 233.4 GPa, respectively.

The stainless steel tubes were seamless tubes supplied by a local producer complying with the ASTM standard (ASTM A959, 2009). The SSTs had two wall thickness specifications (2 and 4 mm) but the same height (500 mm) and outer diameter (219 mm). Three standard coupons were cut from each specification of the SST and tested as per BS 18 (BS 18, 1987). The test curves are shown in **Figure 1**. The key test results are given in **Table 2**, in which the yield strength of stainless steel is taken as 0.2% proof stress (Liao and Ma, 2018a; Liao and Ma, 2018b; Han et al., 2019).

The mix proportions of the SSC are given in **Table 3**. Sea-sand was harvested from the shores near Yingde and Lianzhou, China.

Seawater was simulated using the same ingredients from our previous studies (Zeng et al., 2020a), and the synthesis process followed the ASTM standard D1141 (ASTM D1141, 2013). The SSC was mixed manually in the structural lab of Guangdong University of Technology. According to ASTM C469 (ASTM C469 and C469M-14, 2014), three standard cylinders (150 mm in diameter \times 300 mm in height) were prepared for concrete strength tests. The average compressive strength (f'_{co}), axial strain at the compressive strength (ϵ_c), Young's modulus (E_c), and Poisson's ratio were 52.0 MPa, 0.0028, 34.15 MPa, and 0.20, respectively.

Loading Protocol

The monotonic axial compression load was applied to the specimens continuously until the axial strain reached 10%, whereas the cyclic axial compression involved a number of unloading/reloading cycles. There were three loading protocols considered for cyclic axial compression in this study, which are illustrated in **Figure 2**. Cyclic loading protocol L1 was known as the single full unloading/reloading cycle, that is, at each prescribed unloading strain, only one full unloading/reloading cycle was imposed to the specimens. In this study, the unloading was terminated at a very small load close to zero (i.e., 120 kN, approximately 3.2 MPa) to maintain functionality of the test machine. The reloading was terminated when the reloading strain returned to the prescribed unloading strain. Then, the loading was continued to the next prescribed unloading strain.

Cyclic loading protocol L2 was also concerned with full unloading/reloading cycles. However, L2 was different from L1 such that at each prescribed unloading strain, four repeated full internal unloading/reloading cycles were applied to the specimens, instead of a single full unloading/reloading cycle for L1. The unloading rule for L2 was the same as those for L1, while there were small differences for the reloading rule. For the first three internal cycles ($n \leq 3$), the reloading was terminated when reaching the prescribed unloading strain, and then unloading started for the next internal cycle, whereas for the fourth internal cycle ($n = 4$), when reloading strain recovered to the prescribed unloading strain, the loading was continued to the next prescribed unloading strain.

Cyclic loading protocol L3 was mixed with full and partial repeated unloading/reloading cycles, each with four repeated internal cycles, that is, full repeated unloading/reloading cycles were applied at the first prescribed unloading strain, followed by a partial repeated unloading/reloading cycle at the second prescribed unloading strain, and another full repeated unloading/reloading cycle at the third prescribed unloading strain, and so on. In other words, full repeated unloading/reloading cycles occurred at an odd number of prescribed unloading strains, while partial repeated unloading/reloading cycles occurred at the even numbers. The magnitude of partial unloading was 50% of the applied load at the corresponding prescribed unloading strain. The unloading and reloading rules for the internal cycles of L2 were also applicable for L3. The three cyclic loading protocols can be programmed by the test machine.

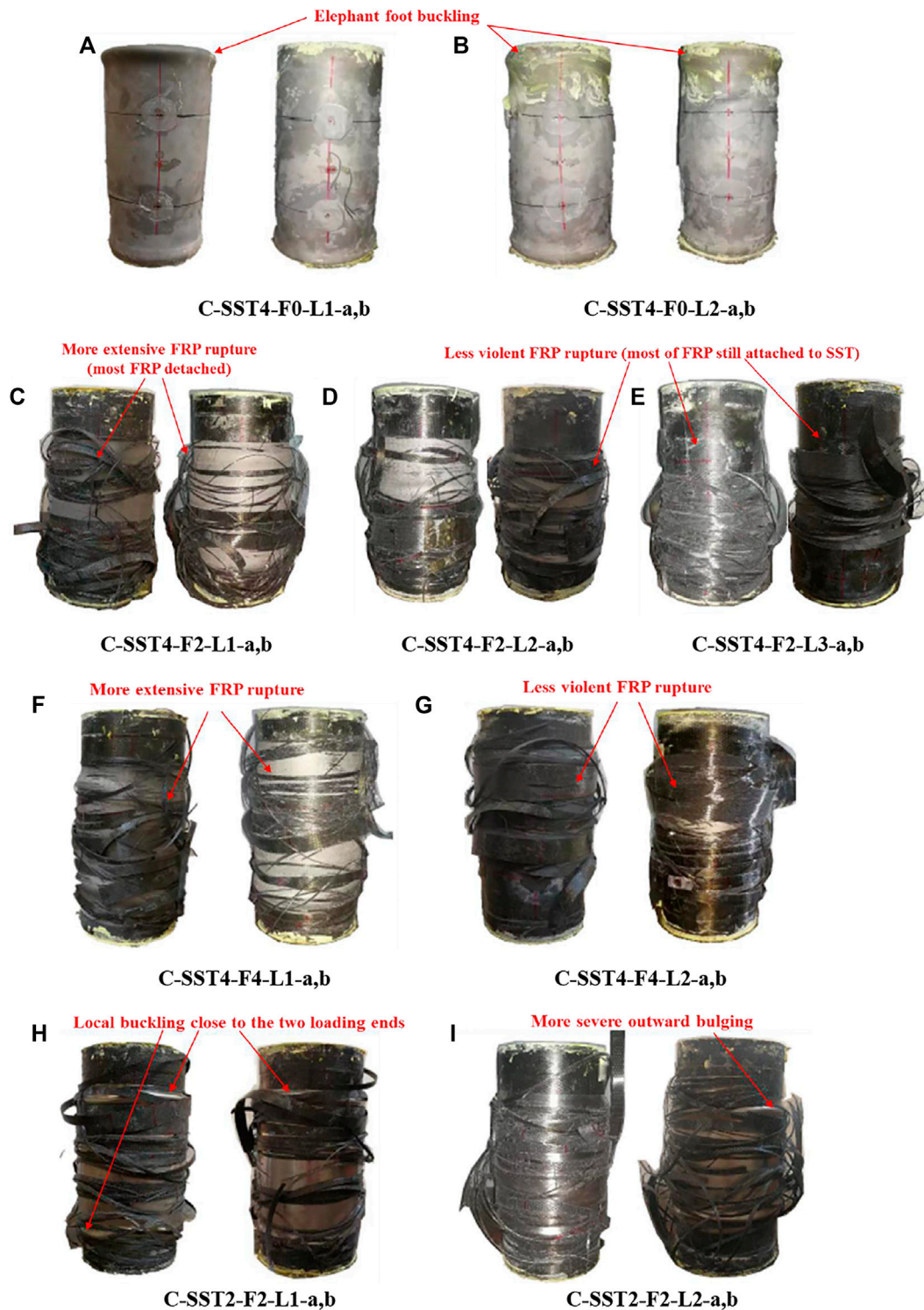


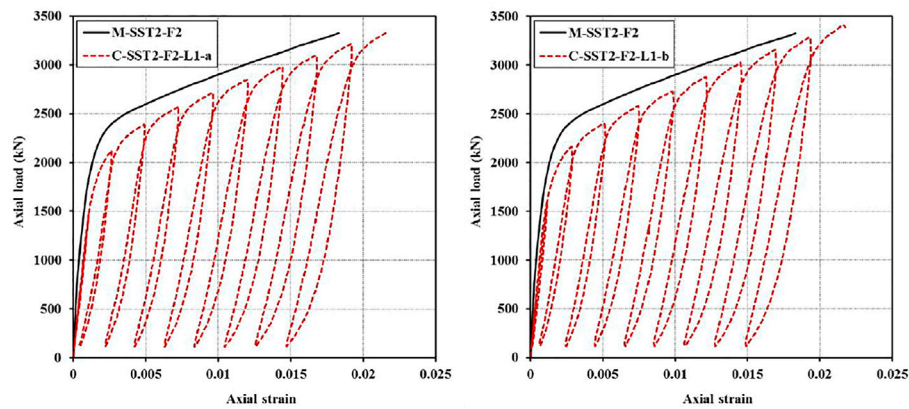
FIGURE 4 | Failure modes for the specimen under cyclic compression. (A) C-SST4-F0-L1-a,b. (B) C-SST4-F0-L2-a,b. (C) C-SST4-F2-L1-a,b. (D) C-SST4-F2-L2-a,b. (E) C-SST4-F2-L3-a,b. (F) C-SST4-F4-L1-a,b. (G) C-SST4-F4-L2-a,b. (H) C-SST2-F2-L1-a,b. (I) C-SST2-F2-L2-a,b.

Test Setup

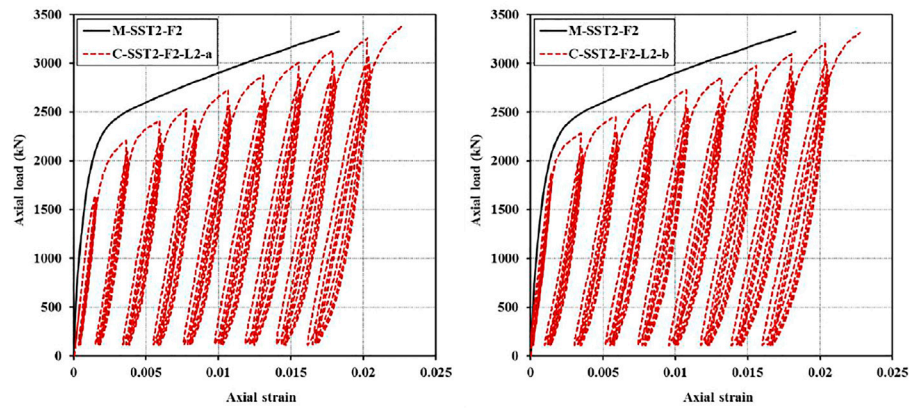
The axial shortening of each specimen was measured by three sets of instruments: 1) four axial strain gages (SGs, gage length

of 20 mm) pasted at the mid-height at every 90° radially (one of the SGs was in the middle of the overlapping zone); 2) four axial linear variable differential transducers (LVDTs) mounted

A SST2-F2 specimens

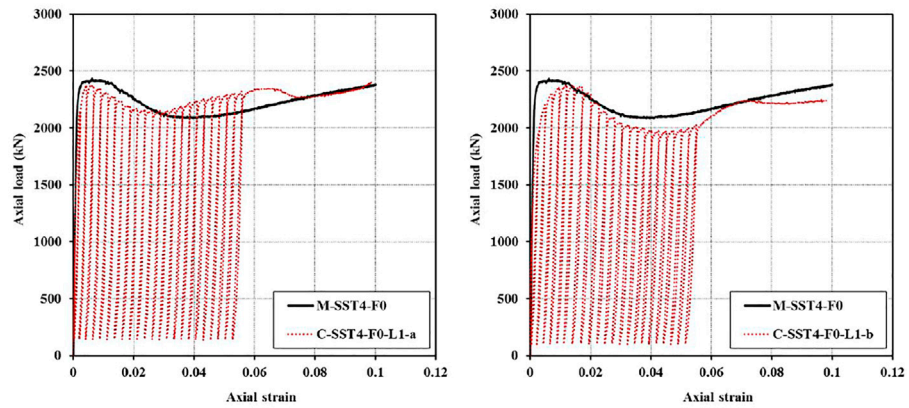


Cyclic loading protocol L1



Cyclic loading protocol L2

B SST4-F0 specimens

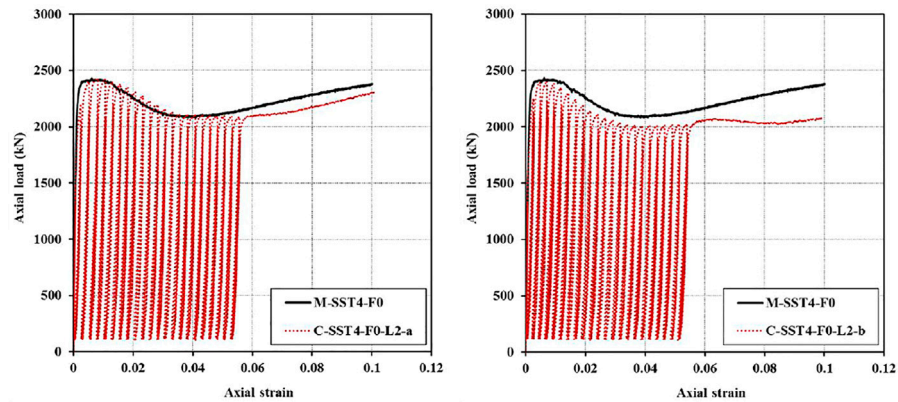


Cyclic loading protocol L1

FIGURE 5 | Axial load–strain curves. (A) SST2-F2 specimens. (B) SST4-F0 specimens. (C) SST4-F2 specimens. (D) SST4-F4 specimens.

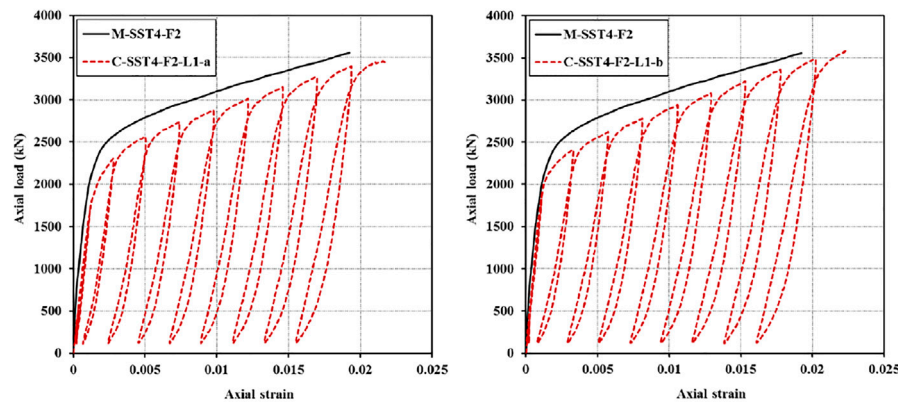
at the same positions of the four axial SGs but over a 200-mm-long region at the mid-height (LVDT-200); 3) another two LVDTs set up between the two loading platens (apart by 180°) to monitor the total shortening over the full height (LVDT-

500). The dilation of the specimens was also recorded by the means of SGs and LVDTs. Four hoop SGs were also glued at the mid-height next to the four axial SGs, but in the horizontal direction. In addition, two horizontal LVDTs set apart by 180°

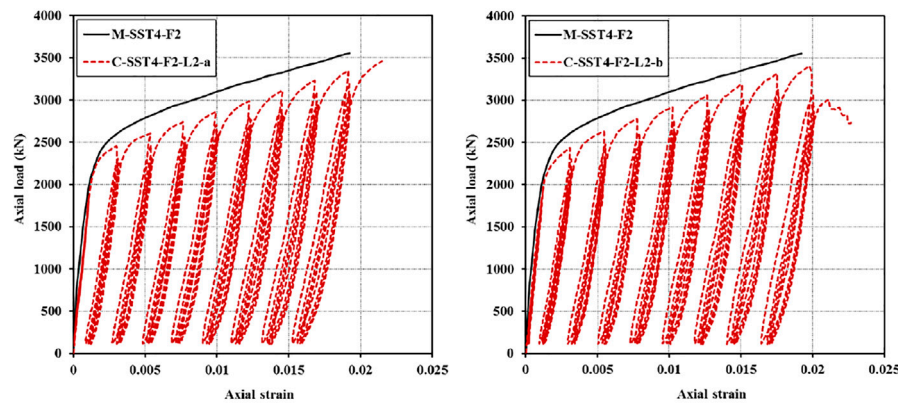


Cyclic loading protocol L2

C SST4-F2 specimens



Cyclic loading protocol L1



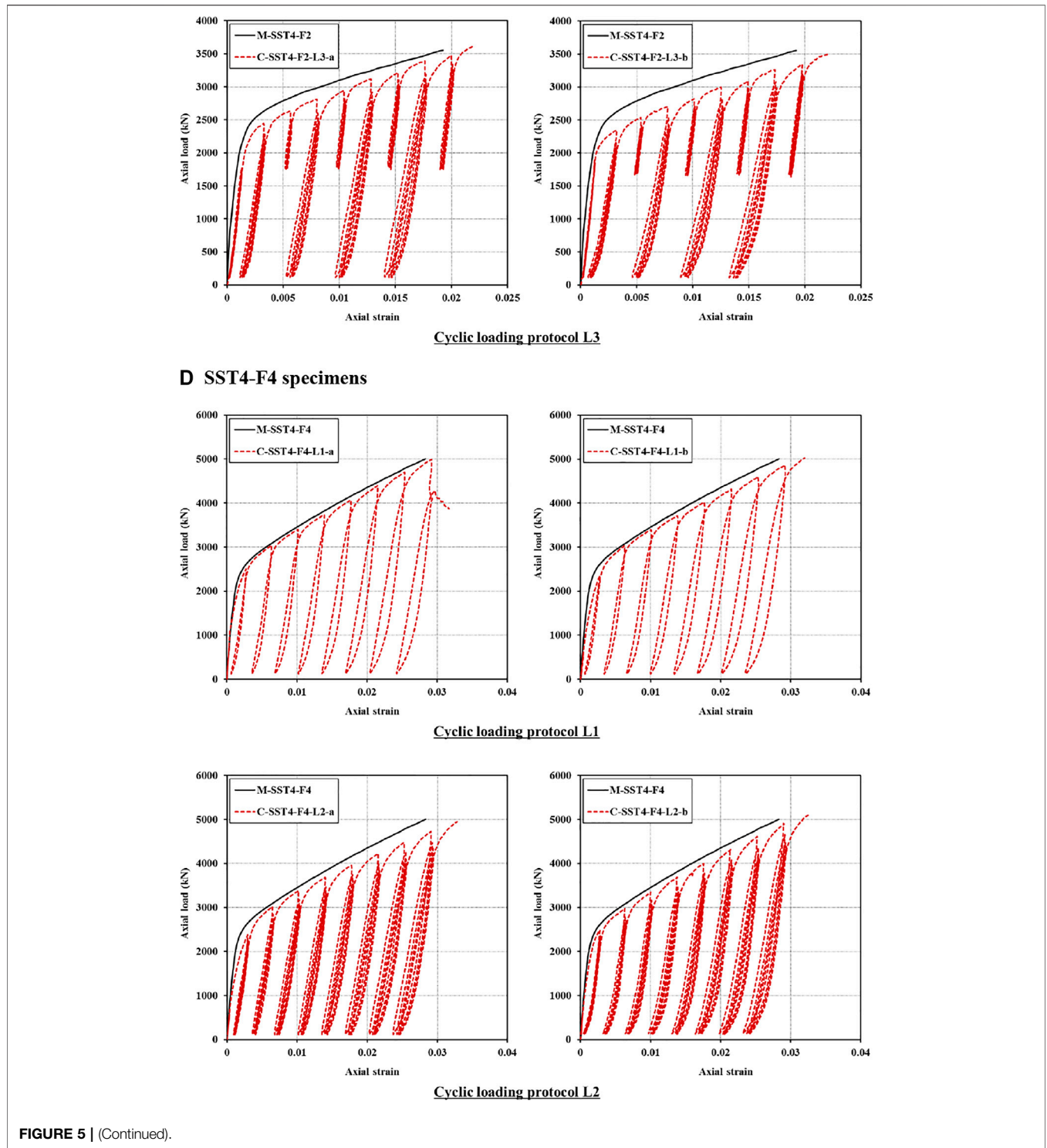
Cyclic loading protocol L2

FIGURE 5 | (Continued).

in the line orthogonal to the two LVDT-500s were also installed. The instrumentation diagram is illustrated in **Figure 3A**.

Before mounting to the test machine, two 50-mm-wide CFRP strengthening strips were applied to both ends of each F-SSCFSSST specimen, while SSCFSST specimens were

left unstrengthened. In addition, thin layers of gypsum mortar were adopted for leveling. The axial compression tests were performed with a 1000-ton compression machine (YAW-10000F); the test setup is shown in **Figure 3B**. Pre-loads up to around 11 MPa were applied to check the functionality of the instruments and the alignments of the loading. The formal



tests were performed with a loading rate of 0.6 mm/min and an unloading rate of 1 mm/min. For SSCFSST specimens, the tests were terminated when axial displacement reached 50 mm (i.e., 10% axial strain), while the tests were terminated when significant FRP rupture occurred for F-SSCFSSST specimens.

TEST RESULTS AND DISCUSSION

Failure Modes

The failure modes of the specimens under cyclic compression are shown in **Figure 4**. It is seen that the two pairs of SSCFSST specimens were subjected to elephant foot buckling at both ends.

TABLE 4 | Summary of key test results.

Specimen	P_{cc} (kN)	ϵ_{cc}	$\epsilon_{cc}/\epsilon_{co}$	$\epsilon_{h,rupt}$
C-SST2-F2-L1-a	3330.1	0.0216	7.71	-0.0137
C-SST2-F2-L1-b	3408.3	0.0218	7.78	-0.0102
C-SST2-F2-L2-a	3372.8	0.0227	8.10	-0.0136
C-SST2-F2-L2-b	3314.2	0.0228	8.13	-0.0150
C-SST4-F0-L1-a	2370.9	0.00436	1.56	\
C-SST4-F0-L1-b	2380.5	0.0120	4.27	\
C-SST4-F0-L2-a	2429.3	0.0078	2.78	\
C-SST4-F0-L2-b	2401.0	0.0071	2.54	\
C-SST4-F2-L1-a	3454.7	0.0218	7.78	-0.0150
C-SST4-F2-L1-b	3591.9	0.0225	8.05	-0.0138
C-SST4-F2-L2-a	3459.6	0.0215	7.68	-0.0132
C-SST4-F2-L2-b	3408.9	0.0227	8.11	-0.0121
C-SST4-F2-L3-a	3606.8	0.0219	7.81	-0.0145
C-SST4-F2-L3-b	3497.6	0.0221	7.91	-0.0115
C-SST4-F4-L1-a	4992.4	0.0317	11.32	-0.0135
C-SST4-F4-L1-b	5024.4	0.0320	11.43	-0.0148
C-SST4-F4-L2-a	4947.0	0.0328	11.72	-0.0134
C-SST4-F4-L2-b	5134.6	0.0327	11.68	-0.0158
M-SST2-F2	3326.0	0.0183	6.54	-0.0119
M-SST4-F0	2425.0	0.0103	3.68	\
M-SST4-F2	3555.8	0.0192	6.87	-0.0125
M-SST4-F4	5006.0	0.0283	10.11	-0.0136

Note: P_{cc} – peak load carrying capacity; ϵ_{cc} – axial strain corresponding to the peak load; $\epsilon_{cc}/\epsilon_{co}$ – axial strain enhancement ratio; $\epsilon_{h,rupt}$ – FRP rupture strain; “\” – not applicable.

This type of failure mode is different from the typical failure mode of CFST specimens reported in the previous studies (Xiao et al., 2005; Xiong et al., 2017; Wang et al., 2018; Wei et al., 2019; Ouyang et al., 2020; Liao et al., 2021a), in which concrete shear failure was the main cause and steel tube buckling tended to occur in both middle upper and middle lower regions, coinciding with the major shear crack of the concrete core. By contrast, elephant foot buckling usually occurs for hollow tubes, and thus the results implied that the bond between the SST and SSC was very weak, especially at the two loading ends. The SST is much smoother than a steel tube, and the cyclic loading would further weaken the bond between the SST and SSC.

For F-SSCFSSST specimens, elephant foot buckling did not occur as both ends of the specimens were sufficiently strengthened. However, local buckling still occurred in the other locations of the SSTs. For specimens confined with 2-ply CFRP sheets, SST local buckling was more frequently seen in the upper or lower regions close to the loading ends, whereas local buckling was less prominent for most of the specimens with 4-ply CFRP wrappings, and the outward expansion was usually at the mid-height region. This observation is consistent with Zhang et al.'s report for FRP-confined CFST specimens (Zhang et al., 2020b), indicating that when confined with FRP jackets, specimens with SST or the conventional steel tube did not have fundamental difference in the failure mode. It is also observed that specimens with a 2-mm-thick SST were subjected to more severe outward bulging because the slenderness ratio of SST2 was twice that of SST4.

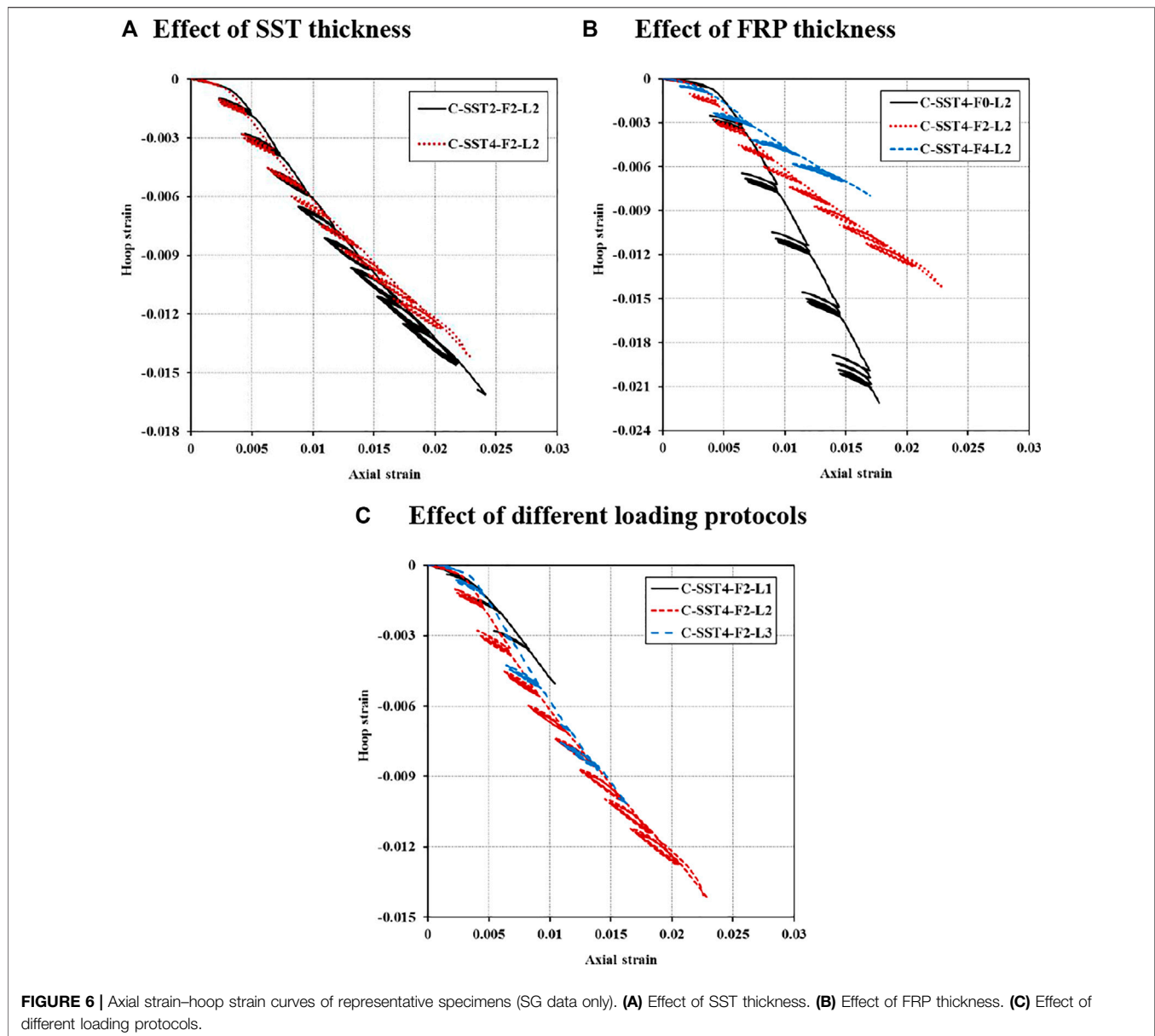
FRP rupture is another characteristic failure mode for F-SSCFSSST specimens. All ruptures occurred at or close to the mid-height region and propagated rapidly to the upper and lower regions simultaneously, unzipping the majority of the CFRP

jacket. When observed carefully, it is revealed that the FRP rupture for specimens under repeated internal cycles (i.e., loading protocol L2 and L3) was less fierce than for those under single cycles (i.e., L1). C-SST4-F2-L3 and C-SST4-F4-L2 specimens were the clear examples that most of the CFRP wrappings were still adhered to the tubes. This could be because the repeated loadings have already caused damages to some FRP wrappings (e.g., some FRP strings already severed), and hence the ultimate FRP rupture was less extensive and drastic.

Axial Load–Strain Behavior

The axial load–strain curves are shown in Figure 5, in which the curves for monotonic and cyclic compression tests are plotted together. The axial strains were obtained as a hybrid record of axial SGs and LVDT-500 (i.e., records were continued with the LVDT-500 data, when SGs malfunctioned), which has been frequently used in a number of similar studies (Zeng et al., 2020a; Zeng et al., 2020b; Zeng et al., 2020c; Zeng et al., 2021a; Ye et al., 2021). The close match of the axial load–strain curves in each pair of duplicated specimens demonstrated the repeatability of the test results. The typical responses of F-SSCFSSST specimens under monotonic compression consisted of three branches (an initial ascending branch representing the elastic response; a transition branch; and a response hardening branch, which can also be treated as a second linear ascending branch), whereas axial load–strain curves of SSCFSST specimens under monotonic compression were subjected to load reductions due to buckling of SSTs.

In terms of cyclic responses, for all three loading protocols, the plastic strains of the specimens increased with the progress of the prescribed unloading strains. The unloading and reloading curve in each cycle can be clearly viewed from loading protocol L1. The reloading curve was almost linear until it reached the new stress point, while the unloading curve was nonlinear, which can be approximated by an almost straight line in the early stage of unloading and a polynomial curve when the applied load was unloaded by around 75%, after which the curvature of the unloading curve became noticeable due to FRP confinement slack (Zeng et al., 2021b). The progressive decreasing slope along the unloading curve in the late stage signified the deterioration of the concrete core. However, the unloading curves for specimens under loading protocol L3 were generally linear, and thus the reloading and unloading curves overlapped with each other. For those specimens under loading protocol L2 and L3, at each prescribed unloading occasion, the plastic strains of the repeated full internal cycles increased marginally with the advancement of internal cycles, and the new stresses recovered to the specific prescribed unloading strain decreased with the increasing internal cycle numbers. Generally, these cyclic responses of F-SSCFSSST columns are similar to the typical cyclic behaviors of the FRP-confined concrete (Lam and Teng, 2009); however, the unloading curve seemed to be less curly in the low stress stage. This is concerned with the plastic strains which are discussed in detail in *Plastic Strain* Section.



When comparing the cyclic responses with monotonic responses for the specimens with the same configurations, it is seen that in each chart, the envelope curve of cyclic response generally matched closely with the monotonic axial load–strain curve (the differences were around 10%). Furthermore, the different cyclic loading protocols (i.e., L1, L2, and L3) seemed to have little impact on the envelope curve of the specimens. This result pattern is consistent with Yu et al.’s findings on FRP-confined CFST columns (Yu et al., 2014) and Lam and Teng’s finding on FRP-confined concrete (Lam and Teng, 2009). Thus, the monotonic axial load–strain curve of an F-SSCFSSST specimen may be taken as the upper bound of the cyclic response of that specific specimen, regardless of the cyclic loading protocols. In addition, using the SSC did not change the general result pattern either; this is

expected as a number of previous investigations have concluded that the short-term mechanical performance between the SSC and conventional concrete casted with the same proportion of freshwater and river sand was minimal (Liao et al., 2022a; Zeng et al., 2022b), and the stress–strain responses of the FRP-confined SSC were also very similar to those of the FRP-confined conventional concrete (Zeng et al., 2020a; Zeng et al., 2020b).

The ultimate loads and axial strains of both monotonically and cyclically loaded specimens are summarized in **Table 4**. It is also noticed that ultimate loads of the specimens with the same configurations also appeared to be independent of cyclic loading protocols. The SST4-F2 specimens were typical examples, in which the ultimate load capacity under monotonic axial compression was 3,555.8 kN. While the ultimate loads extracted from the three cyclic

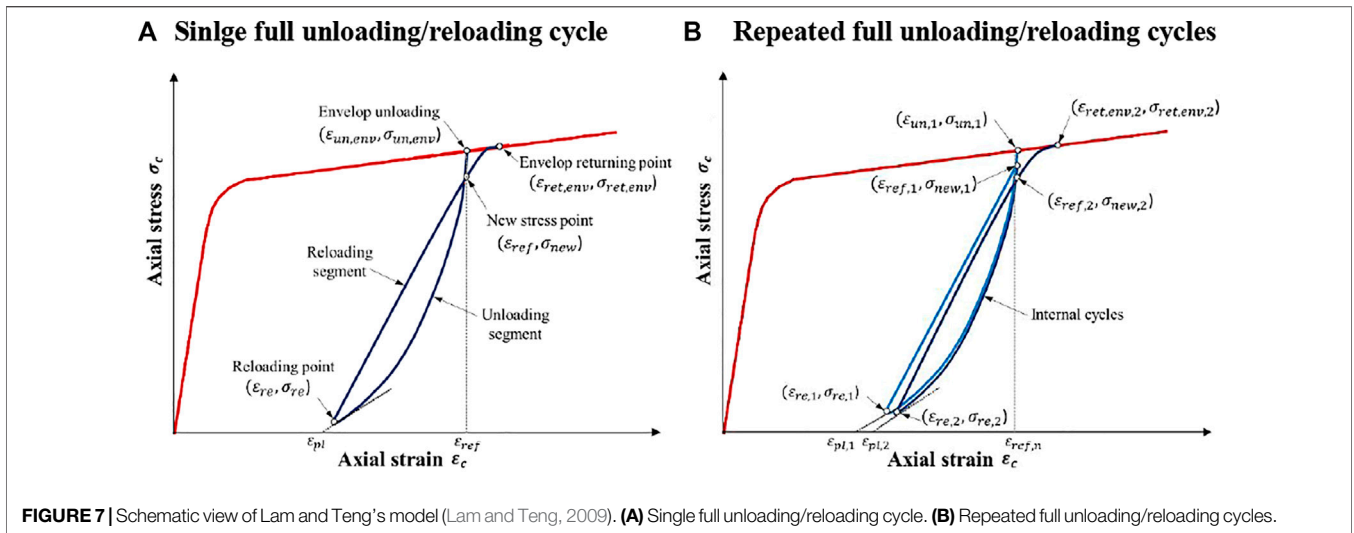


FIGURE 7 | Schematic view of Lam and Teng's model (Lam and Teng, 2009). (A) Single full unloading/reloading cycle. (B) Repeated full unloading/reloading cycles.

loading protocols (i.e., L1, L2, and L3) were 3,523.3, 3,434.2, and 3,552.2 kN, respectively, the maximum difference was just 3.5%.

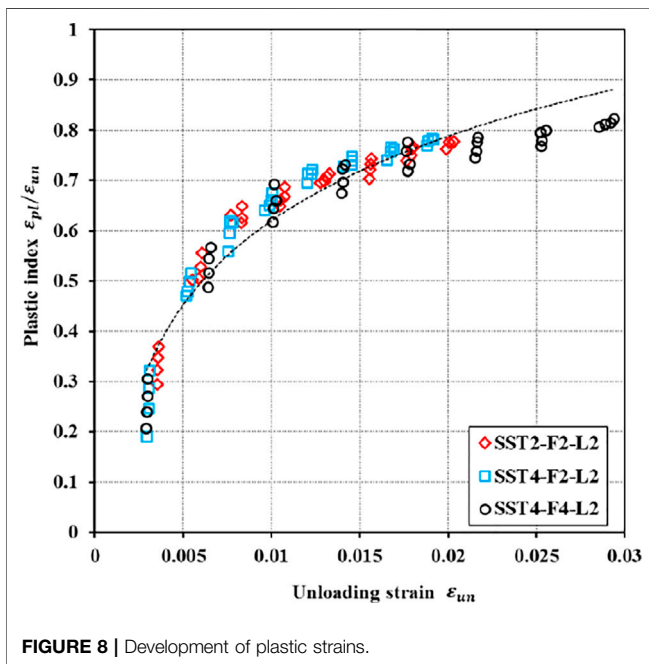


FIGURE 8 | Development of plastic strains.

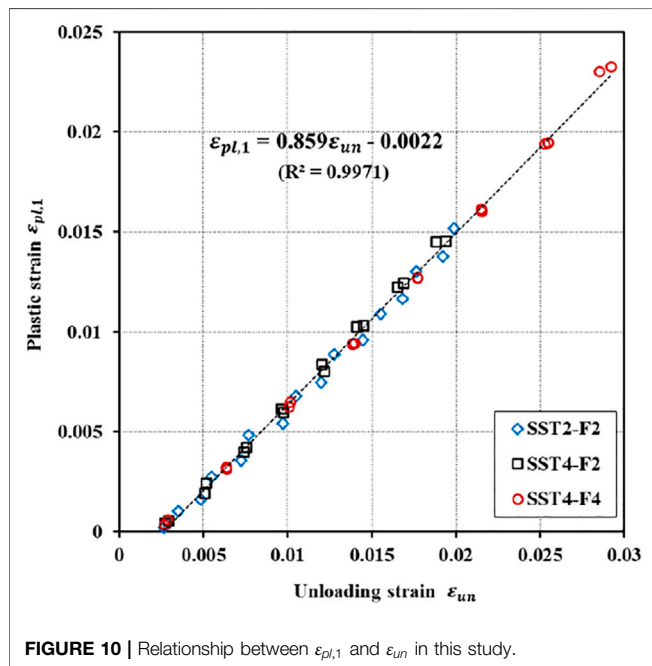
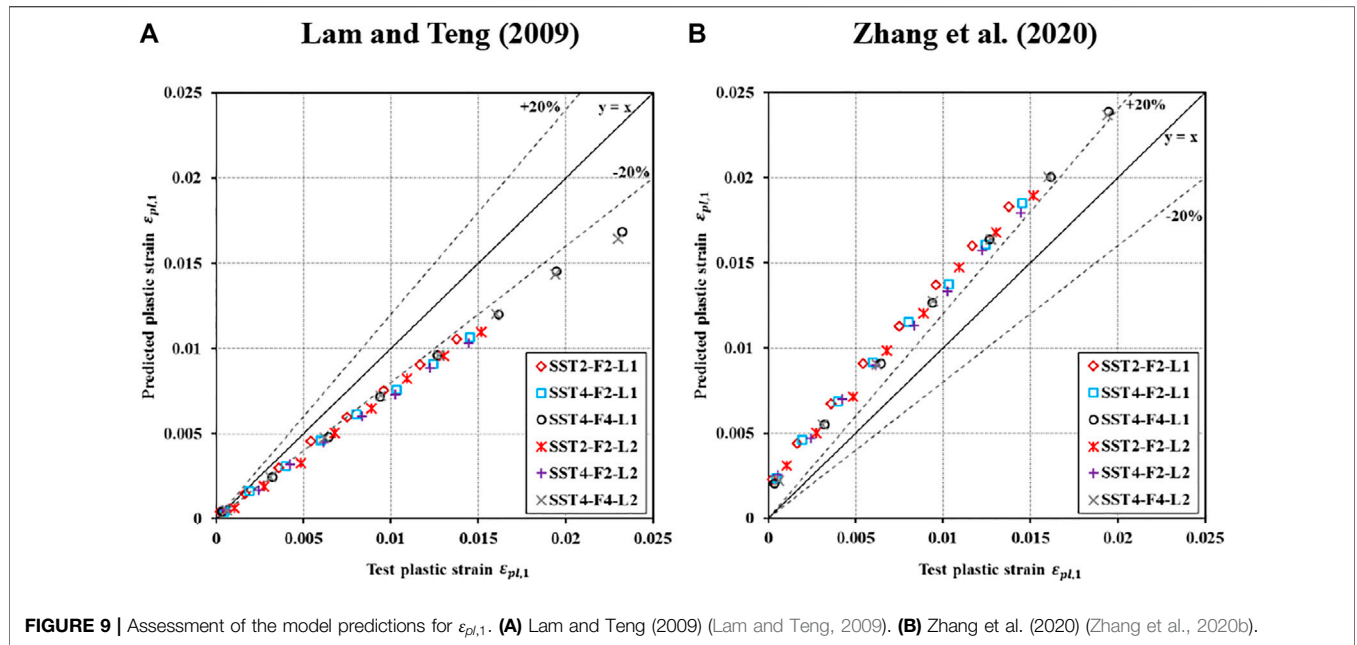
However, the ultimate axial strains of cyclic responses were generally 10–20% greater than those of monotonic curves from their counterparts. The repeated loading can significantly weaken the concrete, making the specimens compacter (i.e., more axial shortening).

Dilation Behavior

The dilation behavior is illustrated by the axial strain–hoop strain curves of some selected specimens in Figure 6. The data of the three

hoop SGs outside of the overlapping zone were used to compute the average hoop strains. The axial strain–hoop strain curves presented in Figure 6 were terminated when hoop SGs were broken. The horizontal LVDTs cannot capture the hoop strain as smoothly as the hoop SGs, and thus LVDT results are not presented. Nevertheless, the data from hoop SGs can still reveal some general result trends.

Similar to the axial load–strain curves, the envelope curve of the cyclic axial strain–hoop strain curves also exhibited a roughly linear relation after the confinements were fully activated. The slope of this roughly linear envelope curve after full activation is a clear indicator for the confinement effect and damage of the concrete core, as the dilation (i.e., concrete cracking) can be restrained. The effect of SST thickness is compared in Figure 6A using C-SST2-F2-L2 and C-SST4-F2-L2 as examples. It is shown that under a particular FRP confinement and the same loading scheme, the dilation curves of these two specimens had very close slopes for the full activation branch, except for the dilation of C-SST2-F2-L2 which was a little larger than that of its counterpart. For example, the maximum hoop strain for C-SST4-F2-L2 before the hoop SG failure was -0.014, while at the same axial strain, the hoop strain of C-SST2-F2-L2 was only 7% greater at -0.015. This result indicates that the confinements provided by the SST were insignificant such that doubling the SST thickness did not lead to noticeable changes in the slope. However, as shown in Figure 6B, increasing FRP confinement thickness can significantly reduce the slope of the envelope curve after full activation when the SST thickness and loading scheme remained the same. A quick assessment using the secant slope at the maximum hoop strains of the three specimens revealed that when comparing to the SST4-F0 specimen, the secant slope has been reduced by 60% for 2-ply FRP jacket and 70% for 4-ply FRP jacket. These results suggested that the confinement effect provided by FRP is much stronger than that of the SST. The damages to the concrete core from different loading schemes can be inferred from Figure 6C using SST4-F2 specimens as examples. It is seen that both L2 and L3 cyclic curves were located below the L1 curve, indicating that increasing internal cycles have caused more damages to the concrete core. When



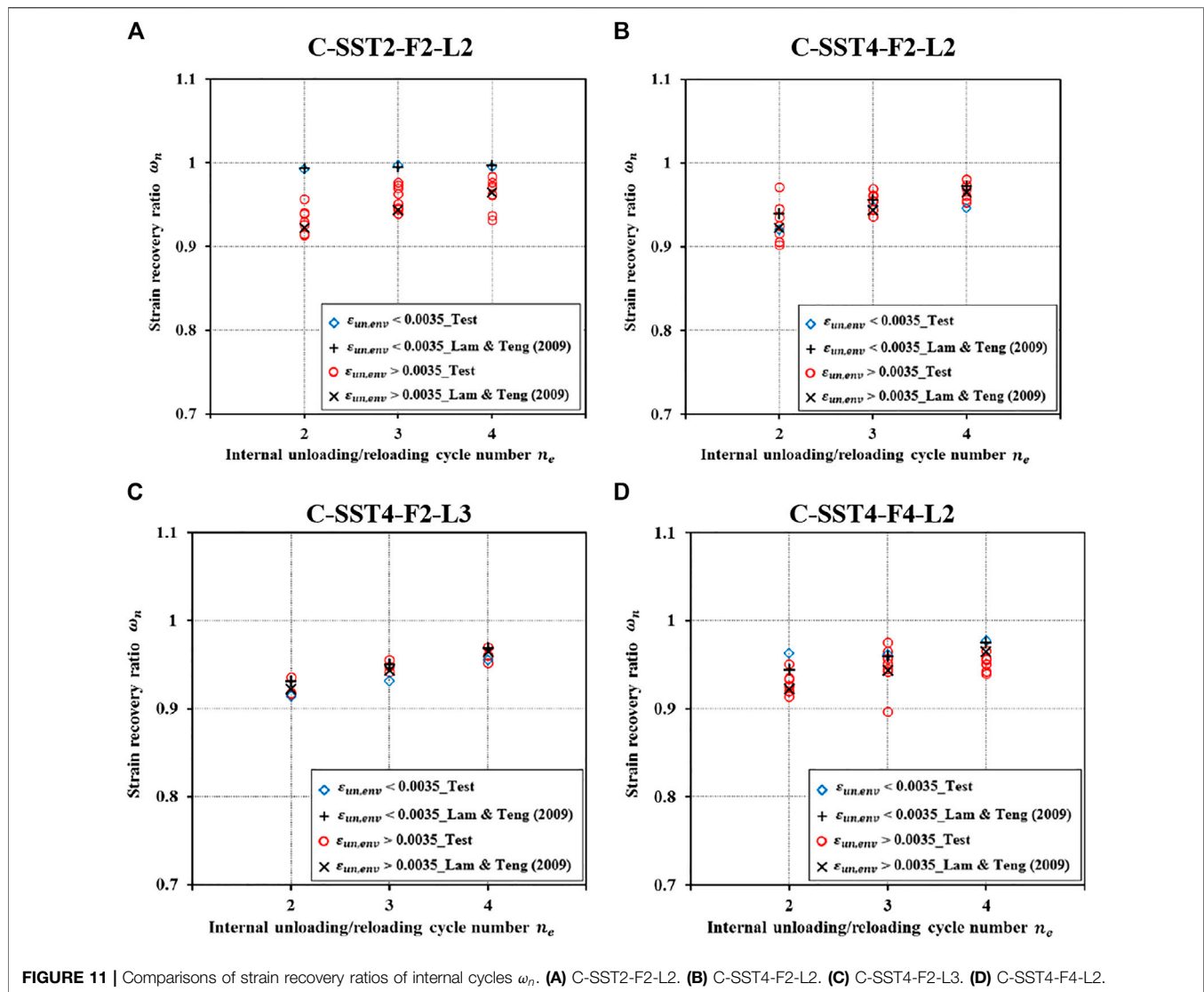
comparing carefully, it is also noticed that the dilations of the L2 curve was a little greater than those of the L3 curve, especially in the early stage of the tests. This is because under partial repeated unloading (L3), the FRP confinement pressure was still high, and thus the cracking could be restrained (Zeng et al., 2021b), while for full repeated unloading (L2), the FRP confinement would sack in the end stage of unloading, during which concrete cracks and crushing

damages tended to occur more easily. However, with the progress of the prescribed unloading strain, the concrete core has been deteriorated to a certain degree such that the dilation between L2 and L3 curves became less noticeable.

ANALYSIS OF KEY PARAMETERS

Note that the key parameters discussed in this section are based on stress-strain curves of confined concrete in F-SSCFSTs. The “stress” is referred to as the average axial stress carried by the concrete core. The axial load carried by the concrete core can be obtained by subtracting the load contribution of SSTs from the total axial load, and the axial stress in SSTs was computed using the plasticity increment theory which has been detailed in our previous study (Zeng et al., 2021a).

Lam and Teng’s cyclic model (Lam and Teng, 2009) is one of the typical models that has good performance and wide applicability. As shown in Figure 7, the cyclic portion of the model can be divided into two segments: an unloading segment and a reloading segment. The unloading segment starts from the prescribed unloading strain ($\epsilon_{un,env}$) and ends at (or close to) the zero-stress point where the reloading segment begins (ϵ_{re}). The unloading curve is modeled by a polynomial equation. The reloading curve is a straight line until the reloading strain recovers to the prescribed unloading strain, in which due to stress deterioration, a new stress point is formed at the prescribed unloading strain. After that, the reloading curve is continued as a parabolic curve returning to the envelope curve to the next prescribed unloading strain. For cyclic responses with internal cycles at each prescribed unloading strain, the behavior is similar, except that the plastic strains and new stress points are renewed at each internal cycle.



The aforementioned behavior is very similar to that observed in the current experimental study. Thus, although Lam and Teng's model (Lam and Teng, 2009) is derived for the FRP-confined concrete, it may still be applicable for the F-SSCFSSST with minor modifications, which can be evaluated by assessing some key model parameters. As briefed above, the reloading points and new stress points are essential to determine the cyclic response curves; therefore, the applicability and performance of Lam and Teng's model (Lam and Teng, 2009) can be evaluated by assessing the accuracy of plastic strains, strain recovery ratios, and stress deterioration ratios.

Plastic Strain

The plastic strain (ϵ_{pl}) is defined as the residual strain corresponding to the zero-stress point in the unloading curve (Lam and Teng, 2009), that is, the strain when the unloading curve intercepts the strain axis. In this study, the plastic strain was obtained by extrapolating the unloading

curve following the curve slope in the final stage, which is illustrated in **Figure 7**.

Using the specimens of loading protocol L2 as examples, the developments of plastic strains are shown in **Figure 8**, in which the plastic index is defined as the ratio of the plastic strain to unloading strain ($\epsilon_{pl}/\epsilon_{un}$) (Zhang et al., 2020b). The plastic index indicates the recovery ability of the specimens. It is shown that the plastic index ranged from 0.2 (for the first prescribed unloading occasion which was usually in the elastic stage of the specimens) to 0.8 (when the FRP jacket ruptured), signifying that the recovery ability of the specimens diminished with the progress of the prescribed unloading strains. The sharp increase in the early stage of the test (i.e., $\epsilon_{un} < 0.01$) suggests that the majority of the damages occurred in the early stage, and thus the concrete core deteriorated rapidly. After that, the strong FRP confinement effect in the hardening stage tended to slow down the increase of the plastic index. It is also interesting

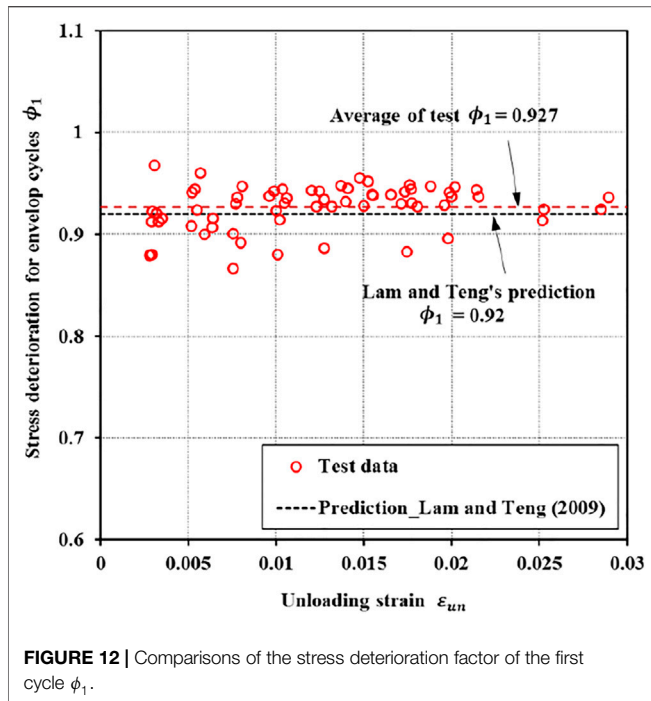


FIGURE 12 | Comparisons of the stress deterioration factor of the first cycle ϕ_1 .

to find out that the plastic strains of the four internal cycles tended to be squeezed together with the progress of the prescribed unloading strains, and this occurred earlier for the specimens with less confinement (i.e., SST2-F2 and SST4-F2 specimens), but much later (i.e., just prior to FRP rupture) for SST4-F2 specimens which had the strongest confinement. This observation again emphasizes the importance of the confining effect of the FRP jacket. When the plastic index reaches 1.0, the unloading curve will become a vertical line, and the specimens showed no recovery ability.

The plastic strain of the envelope cycle ($\epsilon_{pl,1}$) is an important parameter as it not only affects the shape of the unloading curve but also the plastic strains of the following internal cycles. According to Lam and Teng (Lam and Teng, 2009), the plastic strain is dependent on concrete strength (f'_{co}), while it is irrelevant to the FRP thickness. Furthermore, a linear correlation between $\epsilon_{pl,1}$ and ϵ_{un} is also observed in a number of experimental findings (Lam et al., 2006; Zeng et al., 2020d; Zeng et al., 2021b), and an equation has been proposed to predict $\epsilon_{pl,1}$ (Lam and Teng, 2009), which is given in Eq. 1.

$$\epsilon_{pl,1} = \begin{cases} 0, & (0 \leq \epsilon_{un} < 0.001) \\ [1.4(0.87 - 0.004f'_{co}) - 0.64](\epsilon_{un} - 0.001), & (0.001 \leq \epsilon_{un} < 0.0035), \\ (0.948 - 0.004f'_{co})\epsilon_{un} - 0.002, & (0.0035 \leq \epsilon_{un} \leq \epsilon_{cu}) \end{cases} \quad (1)$$

However, the abovementioned findings are concerned with the FRP-confined concrete. Given the dual confinement of the steel tube and FRP jacket, Zhang et al. (Zhang et al., 2020b) considered that the relationship between $\epsilon_{pl,1}$ and ϵ_{un} was no longer linear and proposed a power-law equation to compute $\epsilon_{pl,1}$ for the FRP-confined CFST columns, which was based on their own test data.

As shown in Eqs 2–4, the confinement stiffness of the steel tube (ρ_s) and FRP (ρ_f) is incorporated.

$$\epsilon_{pl,1} = 0.98\epsilon_{un} - 0.0001(\rho_f + 0.27\rho_s)\epsilon_{un}^{0.45}, \quad (0 < \epsilon_{un} \leq \epsilon_{cu}), \quad (2)$$

$$\rho_f = \frac{2E_f t_f}{D f'_{co}}, \quad (3)$$

$$\rho_s = \frac{2E_s t_s}{D f'_{co}}, \quad (4)$$

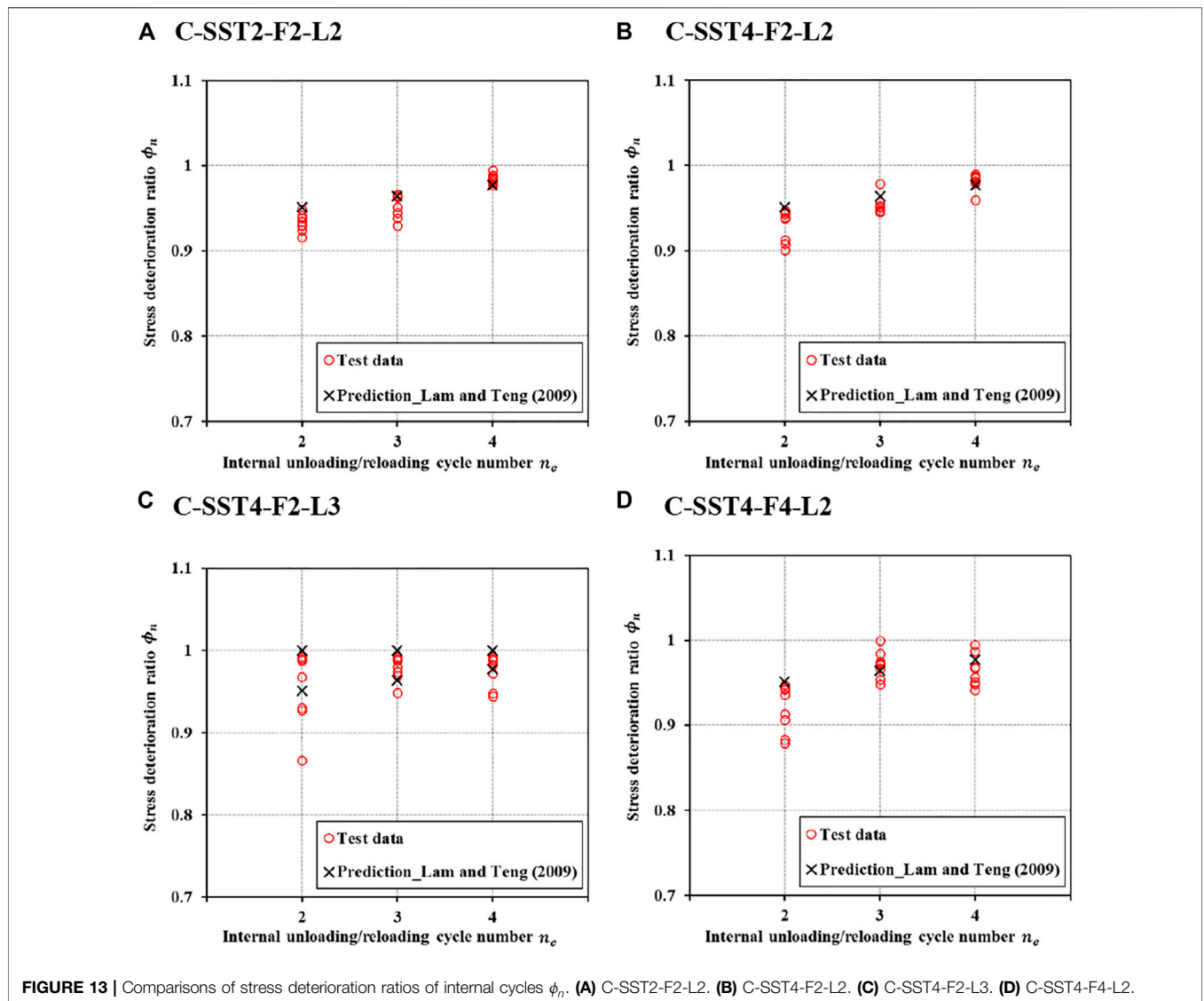
An assessment of the accuracy of the two prediction equations for $\epsilon_{pl,1}$ is given in Figure 9. It is revealed that neither of these two equations can provide accurate predictions. It is interesting to see that Lam and Teng's equation (Lam and Teng, 2009) tended to underestimate all the $\epsilon_{pl,1}$ values by 20%, while overestimations by more than 20% were yielded by Zhang et al.'s equation (Zhang et al., 2020b). Lam and Teng's equation (Lam and Teng, 2009) is a piecewise function for the elastic stage (unloading strain $\epsilon_{un} < 0.0035$), and the predictions were relatively accurate. By comparison, the $\epsilon_{pl,1}$ values in the elastic stage were overestimated more than five times with Zhang et al.'s equation (Zhang et al., 2020b). Apparently, the confinement stiffness of the steel tube (ρ_s) and FRP (ρ_f) should not be included in the formulation for the $\epsilon_{pl,1}$ in the elastic stage as they had not been activated yet, and thus had little effect. As stated earlier, the unloading curve is characterized by a roughly straight line in the early unloading stage and a polynomial curve in the late unloading stage. The underestimations of $\epsilon_{pl,1}$ by Lam and Teng's equation (Lam and Teng, 2009) suggest that compared with the FRP-confined concrete, the polynomial curve in the late unloading stage for F-SSCFST is less curly. This is very likely to be due to the presence of the SST so that the unloading curve is straighter, which is more like the unloading curve of a steel tube. The relationship between $\epsilon_{pl,1}$ and ϵ_{un} in this study is shown in Figure 10. It is evident that the linear relationship between $\epsilon_{pl,1}$ and ϵ_{un} still existed for F-SSCFST, and thus Lam and Teng's equation (Lam and Teng, 2009) could be more reasonable and reliable if the coefficients can be recalibrated for F-SSCFST. A trendline expression has also been given in Figure 10; however, it should be noted that this expression was derived from the concrete strength of 52.0 MPa in this study. More test data with various concrete strengths are required to form a comprehensive database.

Strain Recovery Ratio

The strain recovery ratio ω_n considers the influence of loading history on the plastic strains, which helps determine the plastic strains in the internal unloading/reloading cycles. The ω_n measured from the tests can be written as the following form:

$$\omega_n = \frac{\epsilon_{un,n} - \epsilon_{pl,n}}{\epsilon_{un,n} - \epsilon_{pl,n-1}} \quad (n \geq 2), \quad (5)$$

where $\epsilon_{un,n}$ is the unloading strain of the n^{th} internal unloading/reloading cycle, and $\epsilon_{pl,n-1}$ and $\epsilon_{pl,n}$ are the plastic strain of the $(n - 1)^{\text{th}}$ and the n^{th} internal unloading/reloading cycles, respectively.



In Lam and Teng’s model (Lam and Teng, 2009), ω_n can be computed by Eqs 6–8,

$$\omega_n = \min \left\{ \begin{array}{l} 1 \\ \omega_{n,full} - 0.25(\gamma_{re,n-1} - 1) \end{array} \right\}, \quad (6)$$

$$\gamma_{re,n-1} = \frac{\epsilon_{un,n+1} - \epsilon_{pl,n}}{\epsilon_{ref,n} - \epsilon_{pl,n}}, \quad (7)$$

$$\omega_{n,full} = \begin{cases} 1, & (0 \leq \epsilon_{un,env} < 0.001) \\ 1 + 400(n_e - 0.12)(\epsilon_{un,env} - 0.001), & (0.001 \leq \epsilon_{un,env} < 0.0035) \\ 0.21n_e + 0.88, & (0.0035 \leq \epsilon_{un,env} \leq \epsilon_{cu}) \end{cases}, \quad (8)$$

where $\gamma_{re,n-1}$ is the partial reloading factor; $\epsilon_{ref,n}$ is the reference strain for the n^{th} reloading curve (see Figure 7); $\omega_{n,full}$ is the strain recovery ratio for $\gamma_{re,n-1} = 1$; and n_e is the effective repeated cycles, when $n_e > 6$, $\omega_{n,full} = 1$; otherwise (i.e., $2 \leq n_e \leq 5$), $\omega_{n,full}$ is calculated by Eq. 8.

The ω_n is only concerned with specimens under loading protocol L2 and L3; comparisons of the test and predicted ω_n ratios for the relevant specimens are given in Figure 11 (the ω_n of partial unloading cycles were excluded for C-SST4-F2-L3). It is shown that with the increase of internal unloading/reloading cycles, ω_n would also increase, which means that the development of plastic strain tended to slow down with more internal cycles. This is expected as more repeated cycles would compact the specimen to a steady state. In terms of prediction, Lam and Teng’s model (Lam and Teng, 2009) performed satisfactorily, as the predictions fell in range of the test results. For some cases (e.g., C-SST2-F2-L2 and C-SST2-F4-L2), some predictions were close to the lower bound of the test ω_n ratios, indicating that the predictions would be more conservative (i.e., yielding greater plastic strains for the internal cycles).

Stress Deterioration Ratio

The new stress ($\sigma_{new,1}$) of the envelope cycle on the reloading path crossing the unloading strain is usually less than the envelope unloading stress ($\sigma_{un,env}$). The stress deterioration ratio ϕ_1 is defined as the ratio of $\sigma_{new,1}$ to $\sigma_{un,env}$. For repeated internal unloading/reloading cycles, a more general form for stress deterioration ratio is given in Eq. 9,

$$\phi_n = \frac{\sigma_{new,n}}{\sigma_{ref,n}} \quad (n = 1, 2, 3, \dots), \quad (9)$$

where ϕ_n is the stress deterioration ratio of the n^{th} internal cycle; $\sigma_{new,n}$ is the new stress of the n^{th} internal cycle; $\sigma_{ref,n}$ is the reference stress; and $\sigma_{ref,1} = \sigma_{un,env}$ when $n = 1$, $\sigma_{ref,n} = \sigma_{new,n-1}$ when $n \geq 2$.

Lam and Teng (Lam and Teng, 2009) assumed that ϕ_1 is independent of the unloading strains, and based on a previous study by Lam et al. (Lam et al., 2006), ϕ_1 was set as a constant at 0.92 for $\epsilon_{un} \geq 0.002$. The expression for estimating ϕ_n is given below.

$$\phi_1 = \begin{cases} 1, & (0 \leq \epsilon_{un,env} < 0.001) \\ 1 - 80(\epsilon_{un,env} - 0.001), & (0.001 \leq \epsilon_{un,env} < 0.002), \\ 0.92, & (\epsilon_{un,env} \geq 0.002) \end{cases}, \quad (10)$$

$$\phi_n = \min \left\{ \phi_{n,full} - 0.2(\beta_{un,n} - 1) \quad (n \geq 2), \quad (11)$$

$$\beta_{un,n} = \frac{\sigma_{un,n} - \sigma_{re,n}}{\sigma_{new,n-1}}, \quad (12)$$

$$\phi_{n,full} = \begin{cases} 1, & (0 \leq \epsilon_{un,env} < 0.001) \\ 1 + 1000(0.013n_e - 0.0075)(\epsilon_{un,env} - 0.001), & (0.001 \leq \epsilon_{un,env} < 0.002), \\ 0.013n_e + 0.925, & (0.002 \leq \epsilon_{un,env} \leq \epsilon_{cu}) \end{cases}, \quad (13)$$

where ϕ_n is the stress deterioration for internal cycles; $\beta_{un,n}$ is the partial unloading factor; and $\phi_{n,full}$ is the stress deterioration ratio when $\beta_{un,n} = 1$ (i.e., full unloading, $\sigma_{re,n}$ roughly taken as zero for simplicity). $\phi_{n,full}$ is computed by Eq. 13 when the effective internal cycle number is less than 6 (i.e., $2 \leq n_e \leq 5$) and is taken as 1.0 when $n_e \geq 6$.

Figure 12 plots the test ϕ_1 values against their corresponding unloading strains ϵ_{un} ; it is confirmed that even for F-SSCFSSST, ϕ_1 was also independent of ϵ_{un} . In addition, the average ϕ_1 out of all test data (i.e., 0.927) matched very closely with Lam and Teng's prediction at 0.92 (Lam and Teng, 2009). Furthermore, the stress deterioration ratio predictions in the internal cycles of the relevant specimens are also compared with their test data in Figure 13 (for C-SST4-F2-L3, the ϕ_n values for the partial unloading/reloading cycles are 1.0). Similar to the strain recovery ratio, it is also shown that the stress deterioration ratios in the internal cycles increased gradually with the increase of the repeated internal cycle number. This means that differences of the new stress between the two adjacent cycles became less and less with more repeated internal cycles. This is due to the same reason that the specimen will ultimately reach a steady state under repeated loading. The predictions were also within the range of the test data,

indicating that Lam and Teng's model (Lam and Teng, 2009) is still applicable to F-SSCFSSST with satisfactory accuracy.

CONCLUSION

Axial compression tests were conducted on 22 F-SSCFSSST and SSCFSST specimens in this study, including nine pairs (two identical specimens in a pair) under cyclic compression and four specimens under monotonic compression as references for those under cyclic compression. The effects of SST thickness, FRP thickness, and cyclic loading protocols are under investigation. The failure modes, axial load-strain behavior, and dilation behavior are presented. The applicability and accuracy of Lam and Teng's model (Lam and Teng, 2009) were evaluated and discussed by analyzing three key parameters (plastic strain, strain recovery ratio, and stress deterioration ratio). The key findings are summarized below:

- SSCFSST specimens with no FRP confinement failed from elephant foot buckling at both loading ends, whereas F-SSCFSSST specimens failed from SST local buckling and FRP rupture. FRP rupture was less fierce for F-SSCFSSST specimens with repeated internal unloading/reloading cycles (L2 and L3) than for those with single unloading/reloading cycles (i.e., L1).
- The unloading curve in each cycle was a polynomial curve, while the curvature in the late unloading stage was not prominent due to the presence of SSTs. The reloading curve was almost a straight line before crossing the unloading strain, after which the reloading curve became curly and returned to the envelope curve. The plastic strain increased with more repeated internal unloading/reloading cycles.
- The axial load-strain curves of monotonic compression can be taken as the envelope curve for the cyclic responses as the differences were very small (less than 10%). Different cyclic loading protocols did not affect the ultimate load of a particular specimen obtained from monotonic compression. However, for a particular specimen, the ultimate axial strain of cyclic compression was 10–20% greater than that of monotonic compression.
- The confinement effect of the SST was weak; in comparison, increasing the FRP thickness can substantially restrain the dilations (and damages) of the concrete core. More dilations (and damages) were caused by the cyclic loading with repeated internal unloading/reloading cycles (L2 and L3).
- The envelope plastic strains $\epsilon_{pl,1}$ were linearly correlated to their corresponding unloading strains ϵ_{un} for F-SSCFSSST in this study. Lam and Teng's equation (Lam and Teng, 2009) which is derived for the FRP-confined concrete underestimated the $\epsilon_{pl,1}$ values for F-SSCFSSST by 20%, while Zhang et al.'s equation

(Zhang et al., 2020b), that is based on FRP-confined CFST columns, yielded more than 20% overestimations for $\varepsilon_{pl,1}$ in this study.

- Lam and Teng's model (Lam and Teng, 2009) had satisfactory accuracy in predicting the strain recovery ratios ω_n and stress deterioration ratios ϕ_n for the F-SSCFST in this study.

DATA AVAILABILITY STATEMENT

The original contributions presented in the study are included in the article/Supplementary Material, further inquiries can be directed to the corresponding authors.

AUTHOR CONTRIBUTIONS

J-JZ: conceptualization; funding acquisition; supervision; methodology; roles/writing—original draft; writing—review and

editing. JL: investigation; data curation; roles/writing—original draft; formal analysis. W-FL: investigation and data curation. Y-CG: funding acquisition; project administration; and writing—review and editing. J-KZ: writing—review and editing. J-XL: writing—review and editing. KY: investigation and data curation.

FUNDING

The authors acknowledge the financial support received from the National Natural Science Foundation of China (Grant Nos. 51908137 and 52178277), the Natural Science Foundation of Guangdong Province (Grant Nos. 2019A1515011637 and 2021B1515020029), the Guangzhou Science, Technology, and Innovation Commission (2019040163), and the Guangdong Basic and Applied Basic Research Foundation (2019A1515110808).

REFERENCES

- ASTM A959 (2009). *Standard Guide for Specifying Harmonized Standard Grade Compositions for Wrought Stainless Steels*. Pennsylvania, USA: American Society for Testing Materials.
- ASTM C469 and C469M-14 (2014). *Standard Test Method for Static Modulus of Elasticity and Poisson Ratio of concrete in Compression*. West Conshohocken, USA: ASTM.
- ASTM D1141 (2013). *Standard Practice for the Preparation of Substitute Ocean Water*. West Conshohocken USA: ASTM International.
- ASTM D3039/D3039M-17 (2014). *Standard Test Method for Tensile Properties of Polymer Matrix Composite Materials*. West Conshohocken, USA: ASTM.
- BS 18 (1987). *Tensile Testing of Metals*. London, UK: BSI.
- Dai, P., Yang, L., Wang, J., and Zhou, Y. (2020). Compressive Strength of concrete-filled Stainless Steel Tube Stub Columns. *Eng. Structures* 205, 110106. doi:10.1016/j.engstruct.2019.110106
- Ellobody, E., Young, B., and Lam, D. (2006). Behaviour of normal and High Strength concrete-filled Compact Steel Tube Circular Stub Columns. *J. Constructional Steel Res.* 62 (7), 706–715. doi:10.1016/j.jcsr.2005.11.002
- Geng, Y., Wang, Y. Y., Chen, J., and Zhao, M. Z. (2020). Time-dependent Behaviour of 100% Recycled Coarse Aggregate concrete Filled Steel Tubes Subjected to High Sustained Load Level. *Eng. Struct.* 210, 110353.
- Gholampour, A., and Ozbakkaloglu, T. (2018). Behavior of Steel Fiber-Reinforced concrete-filled FRP Tube Columns: Experimental Results and a Finite Element Model. *Compos. Structures* 194, 252–262. doi:10.1016/j.compstruct.2018.03.094
- Guo, L., Liu, Y., Fu, F., and Huang, H. (2019). Behavior of Axially Loaded Circular Stainless Steel Tube Confined concrete Stub Columns. *Thin-Walled Structures* 139, 66–76. doi:10.1016/j.tws.2019.02.014
- Han, L.-H., Xu, C.-Y., and Tao, Z. (2019). Performance of concrete Filled Stainless Steel Tubular (CFST) Columns and Joints: Summary of Recent Research. *J. Constructional Steel Res.* 152, 117–131. doi:10.1016/j.jcsr.2018.02.038
- Hou, C., Han, L.-H., and Zhao, X.-L. (2014). Concrete-filled Circular Steel Tubes Subjected to Local Bearing Force: Finite Element Analysis. *Thin-Walled Structures* 77, 109–119. doi:10.1016/j.tws.2013.12.006
- Lam, L., Teng, J. G., Cheung, C. H., and Xiao, Y. (2006). FRP-confined concrete under Axial Cyclic Compression. *Cement and Concrete Composites* 28 (10), 949–958. doi:10.1016/j.cemconcomp.2006.07.007
- Lam, L., and Teng, J. G. J. G. (2009). Stress-strain Model for FRP-Confined concrete under Cyclic Axial Compression. *Eng. Structures* 31, 308–321. doi:10.1016/j.engstruct.2008.08.014
- Li, P., and Wu, Y.-F. (2015). Stress-strain Model of FRP Confined concrete under Cyclic Loading. *Compos. Structures* 134, 60–71. doi:10.1016/j.compstruct.2015.08.056
- Liao, J. J., Li, Y. L., Ouyang, Y., and Zeng, J. J. (2021). Axial Compression Tests on Elliptical High Strength Steel Tubes Filled with Self-Compacting concrete of Different Mix Proportions. *J. Build Eng.* 40, 1026788. doi:10.1016/j.job.2021.102678
- Liao, J. J., and Ma, G. (2018). Energy Absorption of the Ring Stiffened Tubes and the Application in Blast wall Design. *Struct. Eng. Mech.* 66 (6), 713–727.
- Liao, J., and Ma, G. (2018). The Blast Alleviation Effects of a Hybrid Barrier System with Triple Energy Absorbers. *Mar. Structures* 61, 540–559. doi:10.1016/j.marstruct.2018.06.018
- Liao, J., Yang, K. Y., Zeng, J.-J., Quach, W.-M., Ye, Y.-Y., and Zhang, L. (2021). Compressive Behavior of FRP-Confined Ultra-high Performance concrete (UHPC) in Circular Columns. *Eng. Structures* 249, 113246. doi:10.1016/j.engstruct.2021.113246
- Liao, J., Zeng, J.-J., Bai, Y.-L., and Zhang, L. (2022a). Bond Strength of GFRP Bars to High Strength and Ultra-high Strength Fiber Reinforced Seawater Sea-Sand concrete (SSC). *Compos. Structures* 281, 115013. doi:10.1016/j.compstruct.2021.115013
- Liao, J., Zeng, J.-J., Gong, Q.-M., Quach, W.-M., Gao, W.-Y., and Zhang, L. (2022b). Design-oriented Stress-Strain Model for FRP-Confined Ultra-high Performance concrete (UHPC). *Construction Building Mater.* 318, 126200. doi:10.1016/j.conbuildmat.2021.126200
- Mo, X.-D., Zeng, W.-Q., Liao, J., and Zeng, J.-J. (2022). Flexural Behavior of Hybrid FRP-concrete-steel Double-Skin Tubular Beams with PBL Shear Connectors. *Eng. Structures* 254, 113840. doi:10.1016/j.engstruct.2022.113840
- Ouyang, Y., Zeng, J., Li, L., and Kwan, A. (2020). Influence of concrete Mix Proportions on Axial Performance of concrete-filled Steel Tubes Made with Self-Compacting concrete. *Adv. Struct. Eng.* 23 (5), 835–846. doi:10.1177/1369433219884457
- Ozbakkaloglu, T., and Akin, E. (2011). Behavior of FRP-Confined normal- and High-Strength concrete under Cyclic Axial Compression. *J. Compos. Construct* 16, 451–463.
- Pan, B., Liu, F., Zhuge, Y., Zeng, J.-J., and Liao, J. (2022). ECCs/UHPFRCCs with and without FRP Reinforcement for Structural Strengthening/repairing: A State-Of-The-Art Review. *Construction Building Mater.* 316, 125824. doi:10.1016/j.conbuildmat.2021.125824
- Qiao, Q., Yang, Z., and Cao, W. (2021). Axial Compressive Behavior of Stainless Steel Tube Confined concrete Column Piers. *Mar. Struct.* 78, 103021.
- Tan, Q.-H., Gardner, L., Han, L.-H., and Song, T.-Y. (2020). Performance of concrete-filled Stainless Steel Tubular (CFST) Columns after Exposure

- to Fire. *Thin-Walled Structures* 149, 106629. doi:10.1016/j.tws.2020.106629
- Tang, H., Chen, J., Fan, L., Sun, X., and Peng, C. (2020). Experimental Investigation of FRP-Confined concrete-filled Stainless Steel Tube Stub Columns under Axial Compression. *Thin-Walled Structures* 146, 106483. doi:10.1016/j.tws.2019.106483
- Tao, Z., Han, L.-H., and Zhuang, J.-P. (2007). Axial Loading Behavior of CFRP Strengthened Concrete-Filled Steel Tubular Stub Columns. *Adv. Struct. Eng.* 10, 37–46. doi:10.1260/136943307780150814
- Teng, J. G., Hu, Y. M., and Yu, T. (2013). Stress-strain Model for concrete in FRP-Confined Steel Tubular Columns. *Eng. Structures* 49, 156–167. doi:10.1016/j.engstruct.2012.11.001
- Wang, W., Sheikh, M. N., Al-Baali, A. Q., and Hadi, M. N. S. (2018). Compressive Behaviour of Partially FRP Confined concrete: Experimental Observations and Assessment of the Stress-Strain Models. *Construction Building Mater.* 192, 785–797. doi:10.1016/j.conbuildmat.2018.10.105
- Wang, Y. H., Nie, J. G., and Fan, J. S. (2013). Theoretical Model and Investigation of concrete Filled Steel Tube Columns under Axial Force-Torsion Combined Action. *Thin-walled Struct.* 69, 1–9.
- Wang, Z.-B., Tao, Z., Han, L.-H., Uy, B., Lam, D., and Kang, W.-H. (2017). Strength, Stiffness and Ductility of concrete-filled Steel Columns under Axial Compression. *Eng. Structures* 135, 209–221. doi:10.1016/j.engstruct.2016.12.049
- Wei, Y., Bai, J., Zhang, Y., Miao, K., and Zheng, K. (2021). Compressive Performance of High-Strength Seawater and Sea-Sand concrete-filled Circular FRP-Steel Composite Tube Columns. *Eng. Structures* 240 (8), 112357. doi:10.1016/j.engstruct.2021.112357
- Wei, Y., Jiang, C., and Wu, Y.-F. (2019). Confinement Effectiveness of Circular concrete-filled Steel Tubular Columns under Axial Compression. *J. Constructional Steel Res.* 158 (7), 15–27. doi:10.1016/j.jcsr.2019.03.012
- Wei, Y., Zhang, Y., Chai, J., Wu, G., and Dong, Z. (2020). Experimental Investigation of Rectangular concrete-filled Fiber Reinforced Polymer (FRP)-steel Composite Tube Columns for Various Corner Radii. *Compos. Structures* 244, 112311. doi:10.1016/j.compstruct.2020.112311
- Wu, Y.-F., and Jiang, C. (2013). Effect of Load Eccentricity on the Stress-Strain Relationship of FRP-Confined concrete Columns. *Compos. Structures* 98, 228–241. doi:10.1016/j.compstruct.2012.11.023
- Xiao, Y., He, W., and Choi, K.-k. (2005). Confined concrete-filled Tubular Columns. *J. Struct. Eng.* 131 (3), 488–497. doi:10.1061/(asce)0733-9445(2005)131:3(488)
- Xiong, M.-X., Xiong, D.-X., and Liew, J. Y. R. (2017). Axial Performance of Short concrete Filled Steel Tubes with High- and Ultra-high- Strength Materials. *Eng. Structures* 136, 494–510. doi:10.1016/j.engstruct.2017.01.037
- Ye, Y.-Y., Liang, S.-D., Feng, P., and Zeng, J.-J. (2021). Recyclable LRS FRP Composites for Engineering Structures: Current Status and Future Opportunities. *Composites B: Eng.* 212, 108689. doi:10.1016/j.compositesb.2021.108689
- Yu, T., Hu, Y. M., and Teng, J. G. (2014). FRP-confined Circular concrete-filled Steel Tubular Columns under Cyclic Axial Compression. *J. Constructional Steel Res.* 94, 33–48. doi:10.1016/j.jcsr.2013.11.003
- Zeng, J.-J., Duan, Z.-J., Gao, W.-Y., Bai, Y.-L., and Ouyang, L.-J. (2020a). Compressive Behavior of FRP-Wrapped Seawater Sea-Sand concrete with a Square Cross-Section. *Construction Building Mater.* 262, 120881. doi:10.1016/j.conbuildmat.2020.120881
- Zeng, J.-J., Gao, W.-Y., Duan, Z.-J., Bai, Y.-L., Guo, Y.-C., and Ouyang, L.-J. (2020b). Axial Compressive Behavior of Polyethylene Terephthalate/carbon FRP-Confined Seawater Sea-Sand concrete in Circular Columns. *Construction Building Mater.* 234, 117383. doi:10.1016/j.conbuildmat.2019.117383
- Zeng, J.-J., Liang, S.-D., Li, Y.-L., Guo, Y.-C., and Shan, G.-Y. (2021a). Compressive Behavior of FRP-Confined Elliptical concrete-filled High-Strength Steel Tube Columns. *Compos. Structures* 266, 113808. doi:10.1016/j.compstruct.2021.113808
- Zeng, J.-J., Liao, J., Ye, Y.-Y., Guo, Y.-C., Zheng, Y., and Tan, L.-H. (2021b). Behavior of FRP Spiral Strip-Confined concrete under Cyclic Axial Compression. *Construction Building Mater.* 295, 123544. doi:10.1016/j.conbuildmat.2021.123544
- Zeng, J.-J., Liao, J., Zhuge, Y., Guo, Y.-C., Zhou, J.-K., Huang, Z.-H., et al. (2022a). Bond Behavior between GFRP Bars and Seawater Sea-Sand Fiber-Reinforced Ultra-high Strength concrete. *Eng. Structures* 254, 113787. doi:10.1016/j.engstruct.2021.113787
- Zeng, J.-J., Ye, Y.-Y., Guo, Y.-C., Lv, J.-F., Ouyang, Y., and Jiang, C. (2020c). PET FRP-concrete-high Strength Steel Hybrid Solid Columns with Strain-Hardening and Ductile Performance: Cyclic Axial Compressive Behavior. *Composites Part B: Eng.* 190, 107903. doi:10.1016/j.compositesb.2020.107903
- Zeng, J.-J., Ye, Y.-Y., Quach, W.-M., Lin, G., Zhuge, Y., and Zhou, J.-K. (2022b). Compressive and Transverse Shear Behaviour of Novel FRP-UHPC Hybrid Bars. *Compos. Structures* 281, 115001. doi:10.1016/j.compstruct.2021.115001
- Zeng, J. J., Zheng, Y. W., Liu, F., Guo, Y. C., and Hou, C. (2020d). Behavior of FRP Ring-Confined CFST Columns under Axial Compression. *Compos. Struct.* 257, 113166.
- Zhang, Y., Wei, Y., Bai, J., Wu, G., and Dong, Z. (2020). A Novel Seawater and Sea-Sand concrete Filled FRP-Carbon Steel Composite Tube Column: Concept and Behaviour. *Compos. Structures* 246, 112421. doi:10.1016/j.compstruct.2020.112421
- Zhang, Y., Wei, Y., Bai, J., and Zhang, Y. (2019). Stress-strain Model of an FRP-Confined concrete Filled Steel Tube under Axial Compression. *Thin-Walled Structures* 142, 149–159. doi:10.1016/j.tws.2019.05.009
- Zhang, Y., Wei, Y., Zhao, K., Ding, M., and Wang, L. (2020). Analytical Model of concrete-filled FRP-Steel Composite Tube Columns under Cyclic Axial Compression. *Soil Dyn. Earthquake Eng.* 139, 106414. doi:10.1016/j.soildyn.2020.106414
- Zhou, J. K., Lin, W. K., Guo, S. X., Zeng, J. J., and Bai, Y. L. (2021). Behavior of FRP-Confined FRP Spiral Reinforced concrete Square Columns (FCFRCS) under Axial Compression. *J. Build Eng.* 45, 103452.

Conflict of Interest: The authors declare that the research was conducted in the absence of any commercial or financial relationships that could be construed as a potential conflict of interest.

Publisher's Note: All claims expressed in this article are solely those of the authors and do not necessarily represent those of their affiliated organizations, or those of the publisher, the editors, and the reviewers. Any product that may be evaluated in this article, or claim that may be made by its manufacturer, is not guaranteed or endorsed by the publisher.

Copyright © 2022 Zeng, Liao, Liang, Guo, Zhou, Lin and Yan. This is an open-access article distributed under the terms of the Creative Commons Attribution License (CC BY). The use, distribution or reproduction in other forums is permitted, provided the original author(s) and the copyright owner(s) are credited and that the original publication in this journal is cited, in accordance with accepted academic practice. No use, distribution or reproduction is permitted which does not comply with these terms.